Journal of Power Sources 215 (2012) 199–215

Contents lists available at SciVerse ScienceDirect

Journal of Power Sources

journal homepage: www.elsevier.com/locate/jpowsour

Impact of particle size ratio and volume fraction on effective material parameters and performance in solid oxide fuel cell electrodes

Benjamin Völker [a,*], Robert M. McMeeking [a,b,c,d]

[a] Department of Mechanical Engineering, University of California, Santa Barbara, CA 93106, USA
[b] Materials Department, University of California, Santa Barbara, CA 93106, USA
[c] School of Engineering, University of Aberdeen, King's College, Aberdeen AB24 3UE, Scotland, UK
[d] INM – Leibniz Institute for New Materials, Campus D2 2, 66123 Saarbrücken, Germany

HIGHLIGHTS

- Particle size and volume fraction in SOFC electrodes strongly influence performance.
- Binary mixtures of spherical electron and ion conducting particles in SOFC analyzed.
- We propose a new estimate for the three-phase boundary reaction domain.
- Parameter study of morphology for enhancement of electrode performance.
- Unlike sized particles in cathode increase SOFC performance up to 15%.

ARTICLE INFO

Article history:
Received 28 February 2012
Received in revised form
30 April 2012
Accepted 9 May 2012
Available online 16 May 2012

Keywords:
Solid oxide fuel cells (SOFC)
Three-phase boundary
Percolation theory
Microstructure
Composite electrode
Multi-physics modeling

ABSTRACT

Optimization of the microstructure of porous electrodes plays an important role in the enhancement of the performance of solid oxide fuel cells. For this, microstructural models based on percolation theory have proven useful for the estimation of the effective material properties of the electrode material, assumed to consist of a binary mixture of spherical electron and ion conducting particles. In this work, we propose an extension of prior approaches for calculating the effective size of the three-phase boundary, which we judge to be physically more sound and, in particular, well suited for characterizing mixtures of particles of different sizes. This approach is then employed in a one-dimensional cell level model encompassing the entire set of processes of gas transport, electronic and ionic conduction as well as the electrochemical reactions. The impact of the electron and ion conducting particle sizes, their volume fraction and their size ratio on the performance of the fuel cell are investigated in a parametric study. Under certain conditions, cathode microstructures having electronic conducting particles of size different from that of the ionic conducting particles become preferable and yield a higher maximum power density when compared to the best possible configuration of monodisperse particles.

1. Introduction

Solid oxide fuel cells (SOFC) directly transform chemical energy from gasified fuels into electrical and heat energy in a highly efficient way. The microstructure of the composite anode and cathode plays a critical role in the high performance of the SOFC. Consisting of binary mixtures of electron and ion conducting particles that form a porous composite, the electrodes must sustain the transport of electrons, ions and the gaseous reactants and products from and to the electrocatalytic active reaction sites, i.e. a small region close to the interface between percolated electronic and ionic particles and exposed to the pore space, known as the three-phase boundary (TPB).

A SOFC's performance is limited by different loss mechanisms. Activation losses occur for the hydrogen oxidation reaction in the anode and the oxygen reduction reaction in the cathode, when electrons are transferred between the respective conduction bands and gas molecular orbitals at the TPB sites. Ohmic losses arise predominantly in the transport of oxygen ions through the electrolyte from the cathode to the anode reaction sites, but also for electron transport between the current collectors and the TPB through the percolated electron conducting particle network. Finally, the diffusive gaseous transport of oxygen through the porous cathode as well as hydrogen and water vapor through the porous anode is governed by concentration losses.

* Corresponding author. Tel.: +1 805 893 4583; fax: +1 805 893 8651.
E-mail address: voelker@engineering.ucsb.edu (B. Völker).

0378-7753/$ – see front matter © 2012 Elsevier B.V. All rights reserved.
doi:10.1016/j.jpowsour.2012.05.014

These loss mechanisms can be directly correlated to the morphological properties of the microstructure. Activation losses are strongly influenced by the disposable reaction sites, i.e. the amount of TPB in the electrodes, which in turn is linked to the respective electronic and ionic conducting particle sizes and volume fractions. Ohmic losses are governed by the effective electronic and ionic resistivites of the porous electrode material that depend strongly on the volume fractions and percolation probabilities of the respective particle networks. The pore radii and porosity, also depending on the particle sizes and volume fractions in the porous electrodes, directly affect the gas transport from the fuel channels to the TBP and consequently the concentration losses. Hence, by optimization of the morphological parameters of the microstructure, i.e. the diameters of the electronic and ionic conducting particles, their size ratios and their volume fractions, the losses can be controlled and the performance of the SOFC can be improved.

For designing highly efficient fuel cell electrodes, the correlation between the parameters of their microstructures and the resulting disposable active TPB for the electrochemical redox reactions is of special interest. Numerical modeling techniques enable us to gain insight into this correlation: One possible approach is to numerically generate electrode microstructures by three-dimensional ordered or disordered packing of spherical particles and subsequently calculate all relevant parameters from these structures [1–4]. In another class of model, which we employ in this work, the SOFC microstructure is described based on an assumed average particle coordination number and percolation theory [5–11]. While the 3D particle packing approach does not need an assumption for a constant average coordination number, it requires extensive computational efforts compared to the approach based on percolation theory. Thus, the latter becomes especially favorable when examining different microstructures having a wide range of particle sizes and volume fractions.

Two different formulations of the effective size of the TPB can be found in literature. They differ in the assumption regarding where the electrochemical reaction takes place. Costamagna et al. [5] introduced the TPB as an area per unit volume (m^2/m^3) parameter, being proportional to the contact area of intersecting electronic and ionic conducting particles. While this first percolation micro-model for SOFCs yields realistic estimates for the TPB size that are successfully employed in a number of theoretical studies [6,8,10–13], it is based on the assumption that the electrochemical reaction happens on the interparticle contact area that is not connected to the pore phase and therefore inaccessible to the gaseous reactants. In contrast, the TPB has also been formulated by Sunde [14] and others [1,7,9,15,16] as a length per unit volume (m/m^3) parameter, hence suggesting that the electrochemical reaction takes place on a (one-dimensional) circular contact line at the intersection of the surfaces of electronic and ionic particles. This approach has been shown to be in good agreement with experiments, i.e. measurements of the TPB length from focussed ion-beam scanning electron microscopy imaging the three-dimensional microstructure [17–20]. It also predicts TPB scaling consistent with experiments, i.e. an increase of the TPB by approximately a factor of four when the particle diameters are reduced by half [21–23]. The drawback of this approach is, however, the assumption that the electrochemical reaction site is hypothetically confined to a one-dimensional line at the interparticle junction. Various recent studies based on density functional theory [24] and models coupling elementary chemistry, electrochemical oxidation reaction kinetics and diffusion mass transport phenomena [25–27] indicate that the electrochemical reaction rather takes place on the particle surfaces within a finite distance from the contact line. In order to accommodate these findings, we propose an extension of the percolation micro-model that is physically sounder by allowing the electrochemical reaction to take place on the particle surfaces within a finite width of the intersection between electronic and ionic particles.

The extended percolation micro-model is then utilized as a foundation for calculating effective material parameters for the porous anode and cathode, such as electronic and ionic conductivities, active three-phase boundary area and mean hydraulic pore radii. Since a main objective of this paper is identifying morphological microstructural parameters that enhance the performance of a SOFC system, an ideal balance among the ohmic, activation and concentration losses is sought. Hence, a one-dimensional cell level model is employed to systematically investigate the impact of the electrode microstructure parameters, such as the electronic and ionic conducting particle diameters and their volume fractions, on the overall performance of the fuel cell system. This model is parameterized through experimental data of Jiang and Virkar [28].

Multiple theoretical studies showing the effect of electrode microstructure on losses in solid oxide fuel cells can be found in literature: Chan and Xia [6] as well as Cannarozzo et al. [13] investigated the influence of anode particle diameter on activation, ohmic and concentration losses, assuming equal sized electronic and ionic particles and the effective material parameters of Costamagna et al. [5]. In their investigation of the overpotentials of cathode interlayers, Chen et al. [17] considered the effect of different particle diameters, size ratios and volume fractions. In addition, there are various parameter studies for microstructure optimization of both conventional [7,10,29] and functionally graded [8,11] electrodes. The main focus in these studies is on finding the ideal thicknesses of anode, dense electrolyte layer and cathode and the ideal particle diameter, while relatively little attention is paid to the effect of the volume fractions and the particle size ratio of the electronic and ionic conducting phases on SOFC performance [30,31]. With only a few exceptions, losses are calculated for only a single constant operating current density, and the effects of specific microstructural properties on losses are examined in an isolated manner for either the anode, electrolyte or cathode rather than addressing the microstructure's impact on the performance of the fuel cell as a whole.

Hence, the main objective of this paper is to systematically investigate the influence of particle diameter, size ratio and volume fraction in anode and cathode on effective material parameters such as TPB, electronic and ionic conductivities and hydraulic pore radii and on the performance of the fuel cell as a whole. Employing our new approach for estimating the extent of the TPB, the impact of morphological parameters on the fuel cell's performance will be demonstrated, and strategies for enhancing the performance will be presented.

2. Method of approach

2.1. Description of anodic and cathodic redox reactions

In this study, we consider an anode-supported SOFC design with single-layer electrodes as shown in Fig. 1. It consists of a nickel-yttria stabilized zirconia (Ni-YSZ) anode serving as the structural support, a YSZ thin-film electrolyte layer and a strontium-doped lanthanum manganite (LSM)-YSZ cathode. Although there are more sophisticated SOFC designs (e.g. reactive bi-layer electrodes [32], functionally graded electrodes [33]), we choose a relatively simple one in order to keep the degrees of freedom in design as low as possible.

The cathode electrode consists of a binary mixture of electronic conducting LSM particles and ionic conducting YSZ particles. Oxygen (O_2) taken from atmospheric air is transported by diffusion

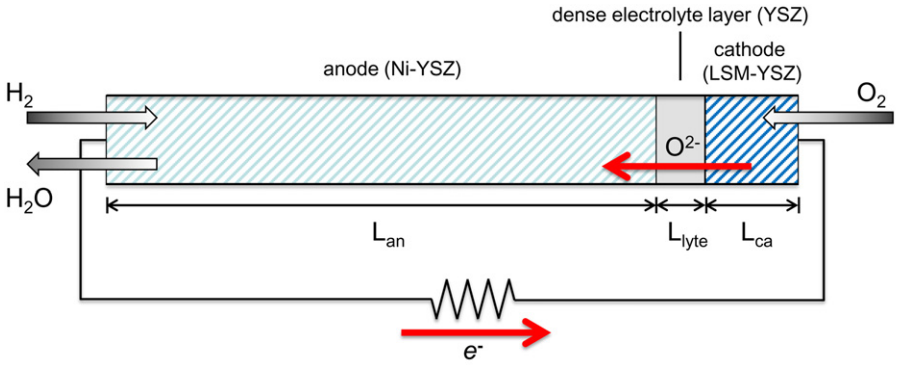

Fig. 1. Schematic of an anode-supported solid oxide fuel cell.

from the cathode gas inlet through the pore phase to TPBs, where the oxygen reduction reaction occurs as

$$\frac{1}{2}O_2 + 2e^- \rightarrow O^{2-}. \quad (1)$$

Electrons are provided from the external circuit, and the oxygen ions produced are transported through the ionic conducting YSZ particle networks and the dense YSZ electrolyte layer towards TPBs in the anode. Besides isolating the anode and cathode for electron conduction, the dense electrolyte layer acts as a gas barrier. In the anode cermet, consisting of electron conducting Ni particles and ion conducting YSZ particles, the hydrogen oxidation reaction takes place as

$$H_2 + O^{2-} \rightarrow H_2O + 2e^-, \quad (2)$$

where hydrogen (H_2) and water vapor (H_2O) are transported to and from the active TPBs by diffusion through pores, and the electrons produced are conducted through the Ni particle network to the current collector where they are provided to the external circuit.

2.2. Effective material properties in anode and cathode

We consider the composite anode and cathode as binary mixtures of spherical particles. Effective microstructure properties such as active TPB size, effective electronic and ionic conductivity and effective pore radii for the gas phase can be determined by using micro-models based on the theory of particle coordination for randomly packed spheres together with percolation theory [5,9]. We start by calculating the disposable active TPB size for electrochemical reactions of a specific microstructure that depends on three major factors:

1. The coordination number, describing the average number of contacts a particular particle in the mixture forms with its neighboring particles. Since the electrochemical reaction takes place at contacting electronic and ionic particles, the average coordination number among particles of different type in a binary mixture is of interest.
2. The percolation probabilities, i.e. the likelihood that particles belong to cluster networks connecting both ends of the configurations, thereby forming a conductive pathway. This takes into consideration that, e.g. in an anode, TPBs are only active for the electrochemical reaction if the electronic particle involved is part of a cluster of the same kind of particles connected to the current collector, and the ionic particle is part of an ion conducting particle network forming a conductive pathway to the dense electrolyte layer.
3. The extent of reaction site per contact pair of unlike particles, given where the electrochemical reaction takes place microscopically at the conjunction of the electron conducting particle, the ion conducting particle and the gas phase.

These factors will be discussed in detail in the following.

2.2.1. Average coordination number

For calculating average coordination numbers and percolation probabilities we will follow closely the work of Chen et al. [9] and only sketch their basic ideas. In contrast to previous micro-models for estimating the coordination number of binary mixtures [34,35], their approach also satisfies the important contact number conservation requirement [5].

In a binary mixture, the surface-area fractions of electron conducting particles, S_{el}, and ion conducting particles, S_{io}, are related to the volume fractions φ_k and the particle radii r_k as

$$S_{el} = \frac{n_{el}4\pi r_{el}^2}{4\pi\left(n_{el}r_{el}^2 + n_{io}r_{io}^2\right)} = \frac{\varphi_{el}/r_{el}}{\varphi_{el}/r_{el} + \varphi_{io}/r_{io}} \quad (3)$$

$$S_{io} = 1 - S_{el}, \quad (4)$$

where n_{el} and n_{io} are the number of electronic and ionic particles per unit volume, respectively. Note that the volume fractions are defined relative to the solid material, so that $\varphi_{el} + \varphi_{io} = 1$. Then, the coordination numbers among particles of the same kind depend on the surface-area fractions as

$$Z_{el-el} = Z_0 S_{el} \quad (5)$$

$$Z_{io-io} = Z_0 S_{io}, \quad (6)$$

where Z_{el-el} describes the average number of contacts of an electron conducting particle with neighboring electron conducting particles, and Z_{io-io} the average number of contacts of an ion conducting particle with neighboring ion conducting particles. The average coordination number of all particles is denoted Z_0 and has a value of 6 for a binary random packing of spheres [5,6,34]. Furthermore, the coordination numbers among particles of unlike kind, relevant for calculating the effective TPB size, can be estimated as

$$Z_{el-io} = Z_0 \frac{\left(1 + (r_{el}/r_{io})^2\right)}{2} S_{io} \quad (7)$$

$$Z_{io-el} = Z_0 \frac{\left(1 + (r_{io}/r_{el})^2\right)}{2} S_{el}. \quad (8)$$

Here, Z_{el-io} is the average number of contacts an electron conducting particle has with ion conducting particles in its vicinity, whereas Z_{io-el} is the number of contacts an ion conducting particle has with electron conducting particles.

2.2.2. Percolation probability

The probability that an electron conducting particle in the binary mixture belongs to a network of similar particles connecting both ends of the configuration can be given as [5,9]

$$P_{el} = \left(1 - \left(\frac{3.764 - Z_{el-el}}{2}\right)^{2.5}\right)^{0.4}, \tag{9}$$

where, according to Kuo and Gupta [36], $Z_{el-el} = 1.764$ represents the percolation threshold. Below this threshold, that depends both on the volume fraction and particle size ratio of electronic and ionic particles, no electric conductive clusters long enough to connect both ends of the configuration will form. Proceeding in the same manner, we can find the probability for a continuous percolating network of ion conducting particles as

$$P_{io} = \left(1 - \left(\frac{3.764 - Z_{io-io}}{2}\right)^{2.5}\right)^{0.4}. \tag{10}$$

2.2.3. Extent of reactive site per contact pair

The main difference between the microstructural percolation models of Costamagna et al. [5] and Chen et al. [9] is how the extent of the reactive site per contact pair is specified, i.e. where the electrochemical reaction is assumed to take place microscopically at the TPB. Costamagna et al. [5], describing the TPB as an area per unit volume (m^2/m^3), assume that the reactive site is the contact area between the electron and ion conducting particle. For the following considerations, it is important to clearly define the contact angle between the involved particles. Without loss of generality, we define the binary mixture of electronic and ionic particles to consist of matrix particles (radius r_{mat}) and inclusion particles of smaller size, i.e. $r_{inc} < r_{mat}$. Then, the circle-like contact area between two particles becomes

$$\alpha_{circ} = \pi r_c^2 = \pi(r_{inc}\sin\theta_{inc})^2, \tag{11}$$

where r_c is the contact radius and θ_{inc} the contact angle of the smaller particle as illustrated in Fig. 2a. In contrast, Chen et al. [9] formulate the TPB in their percolation model as a length per unit volume (m/m^3) as earlier introduced by Sunde [14], stating that the electrochemical reaction takes place on the (one-dimensional) contact perimeter line of overlapping electronic and ionic conducting particles,

$$\alpha_{line} = 2\pi r_c = 2\pi r_{inc}\sin\theta_{inc}. \tag{12}$$

Since various recent studies [24–27] indicate that the electrochemical reaction takes place on the surface of particles within a finite width from the contact perimeter, we propose a new approach for calculating the extent of the reactive site per contact pair. As illustrated in Fig. 2b, the electrochemical reaction is allowed to take place on spherical caps (SPC) up to a distance of x_{inc} from the contact perimeter on the surface of the inclusion particle, and up to a distance of x_{mat} on the surface of the matrix particle:

$$\alpha_{spc} = 2\pi\left(r_{inc}^2\cos\theta_{inc} - r_{inc}^2\cos\left(\frac{x_{inc}}{r_{inc}} + \theta_{inc}\right)\right) + 2\pi\left(r_{mat}^2\cos\theta_{mat} - r_{mat}^2\cos\left(\frac{x_{mat}}{r_{mat}} + \theta_{mat}\right)\right) \tag{13}$$

where θ_{mat} is the contact angle of the matrix particle and given as

$$\theta_{mat} = \arcsin\left(\frac{r_{inc}\sin\theta_{inc}}{r_{mat}}\right). \tag{14}$$

2.2.4. Effective three-phase boundary

Finally, the effective three-phase boundary can be calculated as the product of the extent of reactive sites per electronic and ionic particle contact pair α_x, the total number of contacts between electronic and ionic particles per unit volume, $Z_{el-io}\, n_{el}$, and the likelihood that both electronic and ionic particles belong to percolated clusters $P_{el}\, P_{io}$ as

$$\begin{aligned}\Lambda_x &= \alpha_x \cdot Z_{el-io} n_{el} \cdot P_{el} P_{io} \\ &= \alpha_x \cdot Z_{io-el} n_{io} \cdot P_{el} P_{io},\end{aligned} \tag{15}$$

where

$$n_{el} = \frac{(1-\varepsilon)\varphi_{el}}{(4/3)\pi r_{el}^3} \text{ and } n_{io} = \frac{(1-\varepsilon)\varphi_{io}}{(4/3)\pi r_{io}^3} \tag{16}$$

represent the number of electronic and ionic particles per unit volume [5,7,9] depending on the porosity ϵ, i.e. the volume fraction of the gas phase. As can be seen, the contact number conservation requirement $Z_{el-io} n_{el} = Z_{io-el} n_{io}$ is fulfilled by Eq. (15), and the extent of TPB being available for the electrochemical reactions in an electrode microstructure depends on the volume fractions, the particle radii and the porosity. The subscript x in the definition of Λ

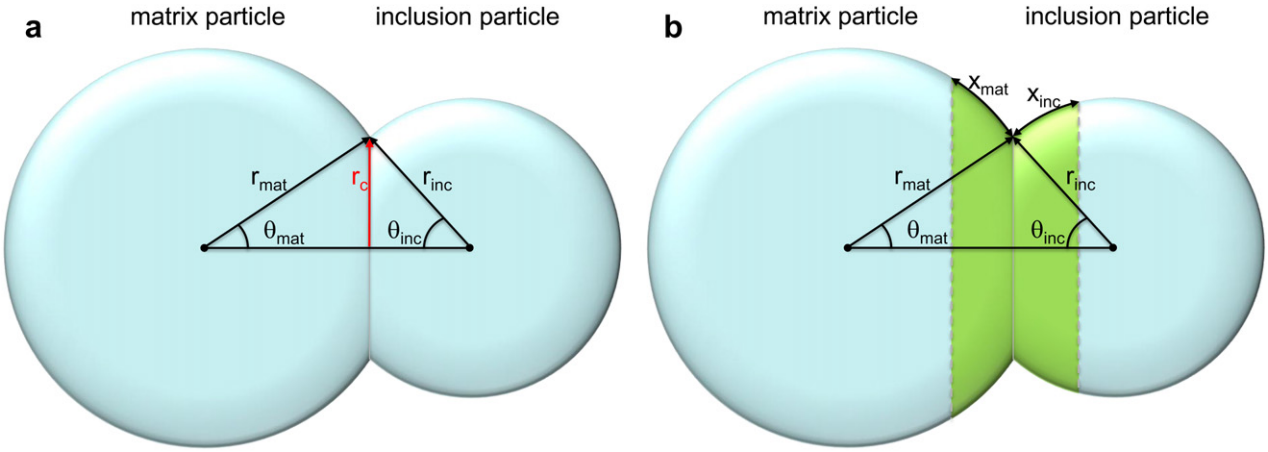

Fig. 2. Geometrical illustration of the different three-phase boundary approaches.

denotes which approach for the amount of reactive sites per contact pair is chosen, i.e. whether α_{circ}, α_{line} or α_{spc} is employed. Thus, the TPB formulations Λ_{circ} and Λ_{spc} are area per unit volume (m^2/m^3) parameters, whereas Λ_{line} is a length per unit volume (m/m^3) quantity.

2.2.5. Effective electronic and ionic conductivity

The effective electronic conductivity σ_{el}^{eff} of a porous electrode depends on its porosity ϵ, the volume fraction φ_{el} of electron conducting particles and the percolation probability P_{el}, i.e. the likelihood that electron conducting pathways form. It can be estimated as

$$\sigma_{el}^{eff} = \frac{1}{\rho_{el}^{eff}} = \sigma_{el}^{0}((1-\varepsilon)\varphi_{el}P_{el})^{\mu} \tag{17}$$

where σ_{el}^{0} is the bulk electronic conductivity. The Bruggeman factor μ takes the effect of tortuous conduction paths into account and is set to a typical value of $\mu = 1.5$ in this study [7,9,29]. Proceeding in the same manner, the effective ionic conductivity can be calculated as

$$\sigma_{io}^{eff} = \frac{1}{\rho_{io}^{eff}} = \sigma_{io}^{0}((1-\varepsilon)\varphi_{io}P_{io})^{\mu}. \tag{18}$$

2.2.6. Effective hydraulic pore radius

In order to include the effect of the microstructure's morphology on the gas diffusion in the porous electrode, a mean hydraulic pore radius is used. According to Cannarozzo et al. [13] it can be written as

$$r_{pore} = \frac{2}{3}\left(\frac{1}{1-\varepsilon}\right)\left(\frac{\varphi_{el}}{r_{el}} + \frac{\varphi_{io}}{r_{io}}\right)^{-1} \tag{19}$$

and depends on the porosity, the volume fractions and particle radii. This effective pore radius will be employed for characterizing the Knudsen diffusion when we model the gas transport.

2.3. One-dimensional cell level model

In order to systematically investigate the impact of the morphological parameters for the anode and cathode on the performance of the SOFC, a one-dimensional cell level model is used. In detail, this model has to consider the following physical phenomena:

- Mass transport of the gaseous species involved through the porous anode and cathode: diffusive transport of reactants from gas channels to the TPB as well as products from reaction sites back to gas channels.
- Electrochemical reactions occurring at the TPB reaction sites.
- Conduction of electrons from reaction sites through the Ni-particle network to the current collector (anode) and from the current collector through the LSM-particle network to TPBs (cathode).
- Ionic transport of oxide ions from cathodic TPBs through the respective YSZ-particle networks and the dense electrolyte layer to anodic TPBs.
- Heat generation caused by ohmic, activation and concentration losses as well as the resulting heat-transport.

Basic assumptions of the model are uniform total gas pressures in the porous anode and cathode, as well as a steady-state operation of the fuel cell, i.e. the gas flows as well as the electronic and ionic currents are time-independent.

2.3.1. Governing equations

The governing equations describing the migration of electrons and ions as well as the gas transport and the heat-transport in anode and cathode electrodes take the form of Poisson equations [6,13,37],

$$\nabla\left(-\frac{1}{\rho_{io}^{eff}}\nabla\Phi_{io}\right) = -\Lambda_n i_n \tag{20}$$

$$\nabla\left(-\frac{1}{\rho_{el}^{eff}}\nabla\Phi_{el,n}\right) = \Lambda_n i_n \tag{21}$$

$$\nabla N_{\alpha} = \frac{\Lambda i_n}{2F} \tag{22}$$

$$\nabla\left(-k_n^{eff}\nabla T\right) = Q_{act,n} + Q_{conc,n} + Q_{joule,n}, \tag{23}$$

where the subscript n denotes the anode or cathode, respectively. Further, the ionic potential Φ_{io}, the electric potential Φ_{el}, the ohmic resistivities ρ^{eff}, the local Faradaic current densities i_n, the rate of mass transport, N_{α}, for gas species α, the Faradaic constant F, the absolute temperature T and the effective thermal conductivities k_n^{eff} are used. The right-hand sides represent the volumetric source terms and describe the conversion of species and charge associated with the electrochemical reactions as well as the generation of heat, Q, due to loss mechanisms such as activation, concentration and ohmic Joule losses. For the dense electrolyte layer separating anode and cathode, all source terms except the Joule heating vanish and the governing transport equations reduce to:

$$\nabla\left(-\frac{1}{\rho_{io,lyte}^{eff}}\nabla\Phi_{io}\right) = 0 \tag{24}$$

$$\nabla\left(-k_{lyte}^{eff}\nabla T\right) = Q_{joule,lyte}. \tag{25}$$

In the following, the modeling of the electrochemical processes, the mass transport and the heat-transport will be discussed in detail.

2.3.2. Electrochemical modeling

The local Faradaic current densities describe the charge transfer rate per unit TPB between the electronic and ionic current correlated with the electrochemical redox reactions in anode and cathode. They can be written in the form of Butler–Volmer equations [6,10,38]

$$i_{an} = i_{an}^{0}\left[\exp\left(\beta_f^{an}\frac{2F}{\overline{R}T}\eta_{an}\right) - \exp\left(-\beta_r^{an}\frac{2F}{\overline{R}T}\eta_{an}\right)\right] \tag{26}$$

$$i_{ca} = i_{ca}^{0}\left[\exp\left(\beta_f^{ca}\frac{2F}{\overline{R}T}\eta_{ca}\right) - \exp\left(-\beta_r^{ca}\frac{2F}{\overline{R}T}\eta_{ca}\right)\right], \tag{27}$$

where β_f and β_r are the forward and reverse charge transfer coefficients in anode and cathode, $\overline{R}$ is the universal gas constant and

$$i_{an}^{0} = \gamma_{an}\left(\frac{p_{H_2}}{p_{H_2}^{ref}}\right)\left(\frac{p_{H_2O}}{p_{H_2O}^{ref}}\right)\exp\left(\frac{-E_{H_2}}{\overline{R}T}\right) \tag{28}$$

$$i_{ca}^{0} = \gamma_{ca}\left(\frac{p_{O_2}}{p_{O_2}^{ref}}\right)^{0.25}\exp\left(\frac{-E_{O_2}}{\overline{R}T}\right) \tag{29}$$

are the reference exchange current densities [12,37,38] having Arrhenius-type relations depending on the local partial gas

pressures of hydrogen (p_{H_2}) and steam (p_{H_2O}) in the anode and oxygen (p_{O_2}) in the cathode. The reference partial gas pressures p^{ref} correspond to the respective gas pressures at the gas inlets, i.e. at the anode's or cathode's surface. Further, E_{H_2} and E_{O_2} are the activation energies for hydrogen oxidation and oxygen reduction, respectively. The parameters γ_{an} and γ_{ca} are used as fitting constants in the model. For the case where Eq. (11) or (13) are employed for calculating Λ, these currents in Eqs. (28) and (29) are per unit TPB area (A m^{-2}), whereas they are currents per unit TPB length (A m^{-1}) if Eq. (12) is used. The irreversible activation losses (also commonly termed "polarization" or "overpotential") required to overcome the reaction barrier energies in anode and cathode are defined as

$$\eta_{an} = E_{an}^{eq} - (\Phi_{io} - \Phi_{el,an}) \tag{30}$$

$$\eta_{ca} = E_{ca}^{eq} - (\Phi_{el,ca} - \Phi_{io}), \tag{31}$$

where

$$E_{an}^{eq} = -\frac{G_{H_2O} - G_{H_2} - G_{O^{2-}}}{2F} + \frac{\overline{R}T}{2F}\log\left(\frac{p_{H_2}}{p_{0,an} - p_{H_2}}\right) \tag{32}$$

$$E_{ca}^{eq} = -\frac{2G_{O^{2-}} - G_{O_2}}{4F} + \frac{\overline{R}T}{4F}\log\left(\frac{p_{O_2}}{p_{0,ca}}\right) \tag{33}$$

are the respective equilibrium potential differences [17] at the reaction interfaces, which are correlated with the local partial gas pressures and the Gibbs free energies G of all species involved. Under equilibrium conditions and in the absence of current flow the SOFC's theoretical open-circuit potential becomes the Nernst value that can be calculated using Eqs. (32) and (33) as

$$V_{Nernst} = -\frac{G_{H_2O} - G_{H_2} - 0.5G_{O_2}}{2F} + \frac{\overline{R}T}{2F}\log\left(\frac{p_{H_2}^{ref}\left(p_{O_2}^{ref}\right)^{0.5}}{p_{H_2O}^{ref}}\right). \tag{34}$$

2.3.3. Modeling of mass transport

When comparing different models for mass transport inside a porous SOFC electrode, Suwanwarangkul et al. [39] came to the conclusion that the dusty-gas model is suited best for simulating the gas transport of a binary gas mixture through a porous medium. It is assumed that the spatial gradient of the total gas pressure in the porous electrodes is insignificant, so that the total gas pressures of the anodic H_2–H_2O system, $p_{0,an} = p_{H_2} + p_{H_2O}$, and the cathodic O_2–N_2 system, $p_{0,an} = p_{O_2} + p_{N_2}$, are constant throughout the whole depth of the electrodes and only diffusive gas transport phenomena have to be taken into account. The dusty-gas model considers two diffusion mechanisms: molecular diffusion is dominant for large pore sizes and high gas pressures, whereas Knudsen diffusion becomes important when pore sizes are much smaller than the mean free path of the gas molecules. As explicitly shown in [40], the effective molecular diffusion coefficient of a gas mixture containing the two components α and β is

$$D_{\alpha\beta}^{eff} = 3/16\left(\frac{\varepsilon}{\tau}\right)\sqrt{\frac{2(\overline{R}T)^3}{\pi}}\sqrt{\frac{1}{M_\alpha} + \frac{1}{M_\beta}}\cdot\left(N_A p_0\left(\frac{\Gamma_\alpha + \Gamma_\beta}{2}\right)^2 \Omega_{\alpha\beta}\right)^{-1} \tag{35}$$

where τ is the tortuosity factor, M the molecular weight and N_A Avogadro's number. Furthermore, the collision integral, which is based on a Lennard-Jones potential [41] becomes

$$\Omega_{\alpha\beta} = \frac{1.06036}{\left(\frac{k_B T}{\xi_{\alpha\beta}}\right)^{0.1561}} + \frac{0.193}{\exp\left(\frac{0.47635 k_B T}{\xi_{\alpha\beta}}\right)} + \frac{1.03587}{\exp\left(\frac{1.52996 k_B T}{\xi_{\alpha\beta}}\right)} + \frac{1.76474}{\exp\left(\frac{3.89411 k_B T}{\xi_{\alpha\beta}}\right)} \tag{36}$$

$$\xi_{\alpha\beta} = \sqrt{\xi_\alpha \xi_\beta} \tag{37}$$

where k_B is the Boltzmann constant and Γ and ξ are the characteristic Lennard-Jones collision diameter and potential energies of the respective gas species [40,42]. On the other hand, the effective Knudsen diffusion coefficient of gas species α, depending on the average pore radius r_{pore}, can be estimated as

$$D_{K,\alpha}^{eff} = 2/3\left(\frac{\varepsilon}{\tau}\right) r_{pore}\sqrt{\frac{8\overline{R}T}{\pi M_\alpha}}. \tag{38}$$

Finally, the rate of mass transport, as predicted by the dusty-gas model for binary gas mixtures [10,39], becomes

$$N_{H_2} = -\frac{1}{\overline{R}T}\left[\frac{1 - \left(1 - \sqrt{M_{H_2}/M_{H_2O}}\right)\frac{p_{H_2}}{p_{0,an}}}{D_{H_2-H_2O}^{eff}} + \frac{1}{D_{K,H_2}^{eff}}\right]^{-1}\nabla p_{H_2} \tag{39}$$

$$N_{O_2} = -\frac{1}{\overline{R}T}\left[\frac{1 - \left(1 - \sqrt{M_{O_2}/M_{N_2}}\right)\frac{p_{O_2}}{p_{0,ca}}}{D_{O_2-N_2}^{eff}} + \frac{1}{D_{K,O_2}^{eff}}\right]^{-1}\nabla p_{O_2}, \tag{40}$$

containing both molecular and Knudsen diffusion mechanisms. Note that due to our previous assumption of constant total gas pressures in the porous electrodes, only p_{H_2} in the anode and p_{O_2} in the cathode have to be considered in the rate of mass transport equations, while the respective remaining partial gas pressures can be calculated as $p_{H_2O} = p_{0,an} - p_{H_2}$ and $p_{N_2} = p_{0,an} - p_{O_2}$.

2.3.4. Thermal modeling

Most SOFC micro-models found in literature are isothermal, assuming a constant temperature profile throughout the whole configuration [6,7,10,17,29], while only a few explicitly take the generation and transport of heat associated with various loss mechanisms into account [43]. In this study we consider heat generation due to activation losses (Q_{act}), concentration losses (Q_{conc}) and ohmic losses, causing Joule heating Q_{joule}. The volumetric heat source terms of the porous electrodes can be written as [43,44]

$$Q_{act,n} = \eta_n \Lambda_n i_n \tag{41}$$

$$Q_{conc,n} = \left(E_n^{eq,ref} - E_n^{eq}\right)\Lambda_n i_n \tag{42}$$

$$Q_{joule,n} = \left(\rho_{io,n}^{eff}\right)^{-1}(\nabla\Phi_{io})^2 + \left(\rho_{el,n}^{eff}\right)^{-1}(\nabla\Phi_{el,n})^2, \tag{43}$$

where the subscript n denotes the anode or cathode, respectively. $E^{eq,ref}$ represents the theoretical open-circuit potential of each electrode, adding up to the Nernst potential $V_{Nernst} = E_{an}^{eq,ref} + E_{ca}^{eq,ref}$ as formulated in Eq. (34). For the dense electrolyte layer only Joule heating due to the ionic current has to be taken into account and the heat generation terms reduce to

$$Q_{\text{joule,lyte}} = \left(\rho^{\text{eff}}_{\text{io,lyte}}\right)^{-1} (\nabla \Phi_{\text{io}})^2. \quad (44)$$

2.3.5. Numerical implementation

In order to numerically solve the governing equations of the one-dimensional SOFC model, the coupled system of partial differential Eqs. (20)–(25) was implemented in the commercial finite-element software COMSOL Multiphysics 3.5a. Representing the degrees of freedom in the finite-element model, Φ_{io}, Φ_{el}, p_{H_2}, p_{O_2} and T are computed in the procedure that is used to integrate the equations and thus describe the solutions of the boundary value problems considered. The respective boundary conditions for the anode and cathode surface are listed in Table 1. For the interior boundaries continuity of flux is ensured.

Throughout this work, the reference temperature is $T_{\text{ref}} = 1073$ K on the exterior boundaries. Under operation conditions, the current density of the cell i_{op} is specified on the exterior boundaries. Then, since the electric potential $\Phi_{\text{el,an}}$ is set to zero on the anode's surface, the value of $\Phi_{\text{el,ca}}$ on the cathode's surface corresponds to the steady-state operating cell voltage $V_{\text{op}}(i_{\text{op}})$.

In order to parameterize the 1D SOFC cell model we use experimental data published by [28], who consider a laboratory anode-supported SOFC button cell operating on H_2 fuel diluted with H_2O vapor and O_2 taken from atmospheric air. All model parameters for the anode, the dense electrolyte layer (DEL) and the cathode were chosen to correspond to the reported experimental values as much as possible and are summarized in Table 2. The mean particle diameters and volume fractions, which were not reported in the original work of Jiang and Virkar [28], are estimated following Jeon et al. [7], who assume a monodisperse mixture of electron and ion conducting particles of equal size and equal volume fractions. On the basis of these model parameters, the effective material parameters of the electrodes are calculated as described in section 2.2. For the effective conductivities of Ni, YSZ and LSM as defined in Eqs. (17) and (18), the temperature-dependent bulk conductivities (in Ω^{-1} m^{-1}) are taken from the literature as [29]

$$\sigma_{\text{YSZ}} = \sigma^0_{\text{io}} = 3.34 \times 10^4 \cdot \exp\left(\frac{-10300\ \text{K}}{T}\right) \quad (45)$$

$$\sigma_{\text{Ni}} = \sigma^0_{\text{el,an}} = 9.5 \times 10^7 \cdot \frac{\exp\left(\frac{-1150\ \text{K}}{T}\right)}{T} \quad (46)$$

$$\sigma_{\text{LSM}} = \sigma^0_{\text{el,ca}} = 4.2 \times 10^7 \cdot \frac{\left(\frac{-1200\ \text{K}}{T}\right)}{T}. \quad (47)$$

Table 1
Exterior boundary conditions used on the anode and cathode surface in the 1D cell model.

Boundary conditions on anode surface
$\Phi_{\text{el,an}} = 0$
$n \cdot \nabla \Phi_{\text{el,an}} = -i_{\text{op}}$
$n \cdot \nabla \Phi_{\text{io}} = 0$
$p_{\text{H}_2} = p^{\text{ref}}_{\text{H}_2}$
$n \cdot \nabla p_{\text{H}_2} = -\frac{\bar{R}Ti_{\text{op}}}{2Fp_{0,\text{an}}} \left(\frac{1 - (1 - \sqrt{M_{\text{H}_2}/M_{\text{H}_2\text{O}}})(p_{\text{H}_2}/p_{0,\text{an}})}{D^{\text{eff}}_{\text{H}_2-\text{H}_2\text{O}}} + \frac{1}{D^{\text{eff}}_{\text{K,H}_2}} \right)$
$T = T_{\text{ref}}$
Boundary conditions on cathode surface
$n \cdot \nabla \Phi_{\text{el,ca}} = i_{\text{op}}$
$n \cdot \nabla \Phi_{\text{io}} = 0$
$p_{\text{O}_2} = p^{\text{ref}}_{\text{O}_2}$
$n \cdot \nabla p_{\text{O}_2} = -\frac{\bar{R}Ti_{\text{op}}}{2Fp_{0,\text{ca}}} \left(\frac{1 - (1 - \sqrt{M_{\text{O}_2}/M_{\text{N}_2}})(p_{\text{O}_2}/p_{0,\text{ca}})}{D^{\text{eff}}_{\text{O}_2-\text{N}_2}} + \frac{1}{D^{\text{eff}}_{\text{K,O}_2}} \right)$
$T = T_{\text{ref}}$

Table 2
Parameters used in the 1D cell model.

Parameter	Anode	DEL	Cathode	Ref.
L [μm]	1100	20	50	[28,37]
p_0 [Pa]	101300		101300	[28]
r_{el} [nm]	500		500	[7,28]
r_{io} [nm]	500		500	[7,28]
φ_{el}	0.5		0.5	[7,28]
φ_{io}	0.5		0.5	[7,28]
ε	0.4		0.4	[32,37]
τ	5		5	[32,37]
θ_{inc} [°]	15		15	[5]
β_{f}, β_{r}	0.5		0.5	[38]
k^{eff} [Wm^{-1}K^{-1}]	11	2.7	6	[43]
M_{H_2} [mol^{-1}kg]	$2.016.10^{-3}$			
$M_{\text{H}_2\text{O}}$ [mol^{-1}kg]	$18.02.10^{-3}$			
M_{O_2} [mol^{-1}kg]			$32.00.10^{-3}$	
M_{N_2} [mol^{-1}kg]			$28.01.10^{-3}$	
ξ_{H_2} [K]	59.7			[10,42]
$\xi_{\text{H}_2\text{O}}$ [K]	809.1			[10,42]
ξ_{O_2} [K]			106.7	[10,42]
ξ_{N_2} [K]			71.4	[10,42]
Γ_{H_2} [Å]	2.827			[10,42]
$\Gamma_{\text{H}_2\text{O}}$ [Å]	2.641			[10,42]
Γ_{O_2} [Å]			3.467	[10,42]
Γ_{N_2} [Å]			3.798	[10,42]
E_{H_2} [J mol^{-1}]	$120{,}10^3$			[17]
E_{O_2} [J mol^{-1}]			$130 \cdot 10^3$	[17]
G_{H_2} [J mol^{-1}]	$-147.1\ 10^3$			[37]
$G_{\text{H}_2\text{O}}$ [J mol^{-1}]	$-454.9 \cdot 10^3$			[37]
G_{O_2} [J mol^{-1}]			$-228.0 \cdot 10^3$	[37]
$G_{\text{O}^{2-}}$ [J mol^{-1}]	$-236.4 \cdot 10^3$		$-236.4 \cdot 10^3$	[37]
x_{inc}, x_{mat} [nm]	29.2		29.2	
γ_{circ}, γ_{spc} [A m]	$1.13 \cdot 10^5$		$1.41 \cdot 10^4$	
γ_{line} [A m^{-1}]	$7.31 \cdot 10^{-3}$		$9.12 \cdot 10^{-4}$	
$\Lambda_{\text{circ},0}$ [m^{-1}]	$8.38 \cdot 10^5$		$8.38 \cdot 10^5$	
$\Lambda_{\text{line},0}$ [m^{-2}]	$1.30 \cdot 10^{12}$		$1.30 \cdot 10^{12}$	
$\Lambda_{\text{spc},0}$ [m^{-1}]	$8.38 \cdot 10^5$		$8.38 \cdot 10^5$	

By utilizing α_{circ} from Eq. (11) and α_{line} from Eq. (12), we calculate the effective extent of TPB for the morphological parameters listed in Table 2 and defined in Eq. (15), both as an area per unit volume quantity $\Lambda_{\text{circ},0}$ (m^2/m^3) and a length per unit volume quantity $\Lambda_{\text{line},0}$ (m/m^3). Then, by using a best-fitting approach, we adjust the parameters of our model, $\gamma_{\text{circ,an}}$, $\gamma_{\text{circ,ca}}$ and $\gamma_{\text{line,an}}$, $\gamma_{\text{line,ca}}$ in Eqs. (28) and (29) to the experimental data reported by Jiang and Virkar [28]. Finally, the constants x_{inc} and x_{mat} in Eq. (13), defining the distance from the contact perimeter that is electrochemically active on contacting electronic and ionic particles (see section 2.2.3) are chosen in such a way that the reactive area per contact pair α_{spc} is in agreement with α_{circ}, and consequently $\Lambda_{\text{spc}} = \Lambda_{\text{circ}}$. Fig. 3 provides comparisons between results of the numerical 1D SOFC model and experimental data reported by Jiang and Virkar [28] that was used to parameterize this model.

While a good agreement is achieved for higher current densities, i.e. in the operating range close to the maximum power density, there are some deviations between experiment and model near the open-circuit voltage. Similar findings have been reported and discussed by Grew et al. [37], who explain the deviations by possible fuel leakage in the experiment and/or pinholes in the dense electrolyte layer. Other possible contributions to the deviation might lie in the nature of the percolation micro-model that assumes a constant coordination number of 6, as well as in capturing the electrochemical reactions by use only of the Butler–Volmers equation. Furthermore, as reported by Kenney et al. [1], the assumption of uniformly sized, monodisperse electron and ion conducting particles in both electrodes leads to higher TPB when compared to particle mixtures of distributed sizes as found in real electrodes.

3. Results and discussion

3.1. Comparison of different TPB formulations

In a first step we compare the three geometrical approaches shown in section 2.2.3 for calculating the extent of electrochemically reactive sites Λ_{circ}, Λ_{line} and Λ_{spc}, especially regarding their differing scaling behavior. For the morphological parameters $r_{el} = r_{io} = 500$ nm and $\varphi_{el} = \varphi_{io} = 0.5$ the calculated reference values of Λ_0 are listed at the bottom of Table 2. The values found for x_{inc} and x_{mat} of about 30 nm are in agreement with findings from studies based on density functional theory [24] and models coupling elementary chemistry, electrochemical oxidation reaction kinetics and diffusion mass transport phenomena [26,27], which indicate that depending on the exact reaction mechanism in the electrochemistry, the reaction takes place up to a few tens of nanometers, but less than 100 nm [25] from the contact perimeter line between electron and ion conducting particles.

For a mixture of electron and ion conducting particles of the same size ($r_{el} = r_{io}$) and equal volume fraction ($\varphi_{el} = \varphi_{io} = 0.5$), the scaling of Λ with particle size is shown in Fig. 4.

In order to ensure comparability between the different approaches, the TPB is normalized by the respective reference values Λ_0 from Table 2. Significant differences in the scaling behavior are found: Λ_{circ} is inversely proportional to the particle size, $\Lambda_{circ} \propto r^{-1}$, while Λ_{line} shows an inverse quadratic behavior, $\Lambda_{line} \propto r^{-2}$. In contrast, the scaling behavior with the new TPB approach, Λ_{spc}, coincides with Λ_{line} for relatively big particle sizes, i.e. when the particle radii r_{el}, r_{io} are much larger than the electrochemically active domains x_{inc}, x_{mat} on the particles' surfaces, but shows an increasing deviation for smaller particle sizes, where $\Lambda_{spc} \propto r^{-b}$, $b > 2$.

Of special interest is the TPB's scaling behavior in binary particle mixtures with electron and ion conducting particles of different size. We define the particle size ratio

$$R = r_{io}/r_{el} \tag{48}$$

as the ratio of the radius of the ion conducting particles to the radius of the electron conducting particles. We then select for study three values of the particle size ratio, R, namely $R = 0.5, 1$ & 4. For

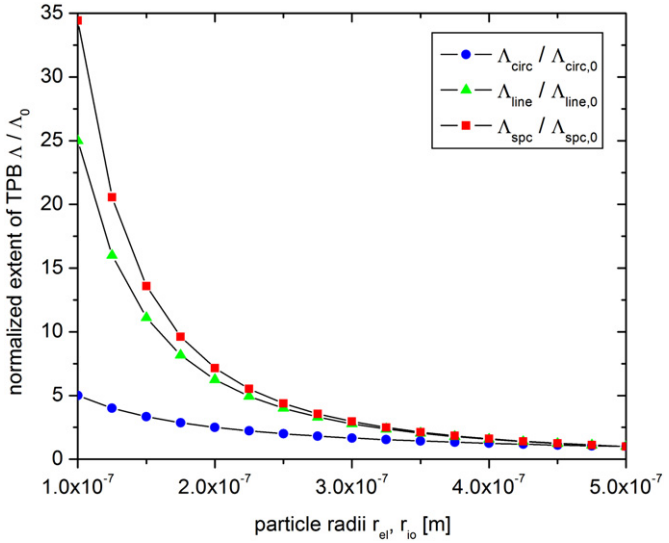

Fig. 4. Three-phase boundary scaling behavior for monosized particle mixtures ($r_{io} = r_{el}$) with identical volume fractions ($\varphi_{el} = \varphi_{io} = 0.5$): comparison of the three-phase boundary measures Λ_{circ}, Λ_{line} and Λ_{spc}.

better comparability of the results obtained by the different approaches, we further introduce the mean particle radius of the binary mixture as

$$\bar{r} = \varphi_{io} r_{io} + \varphi_{el} r_{el} \tag{49}$$

i.e. the volume fraction weighted average of the particle radii.

Fig. 5a shows the normalized extents of the TPBs, Λ_{circ}, Λ_{line} and Λ_{spc} from Eq. (15) for three mixtures of different particle size ratios. The electron and ion conducting particle radii are chosen in such a way that the mean particle radius of each binary mixture is the same and equal to 500 nm for the volume fraction of the electron conduction particle φ_{el}^{max} where the maximum for Λ occurs. As a consequence, the particle sizes are computed as

$$r_{el} = \frac{\bar{r}}{\left(1 - \varphi_{el}^{max}\right) R + \varphi_{el}^{max}} \text{ and } r_{io} = R r_{el}. \tag{50}$$

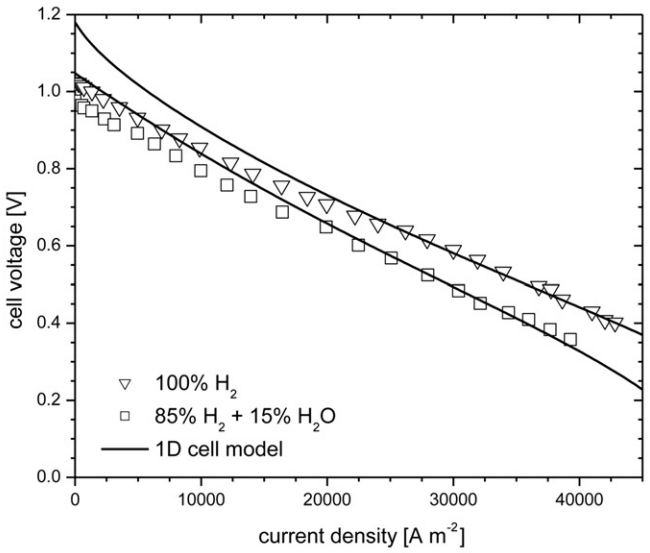

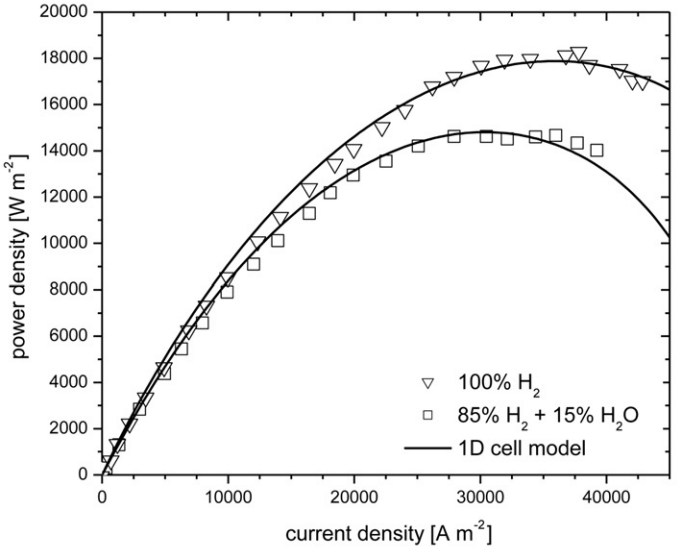

Fig. 3. Comparison between results of the 1D cell model and experimental data by [28].

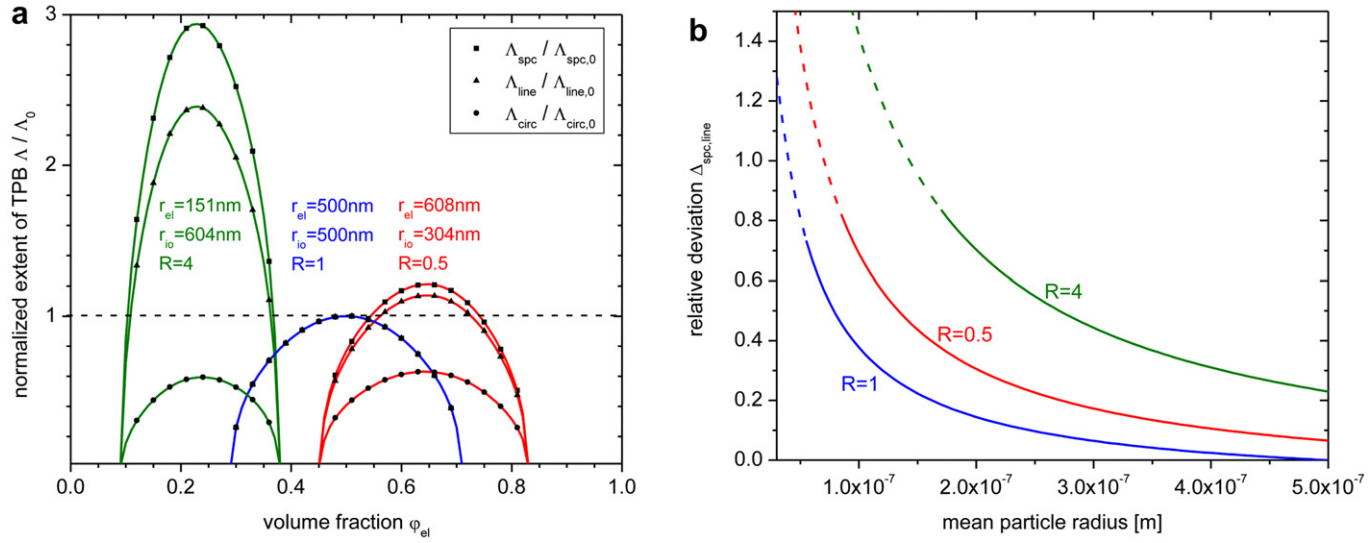

Fig. 5. Comparison of the scaling behavior for the different three-phase boundary measures. (a) For a mean particle radius of $\bar{r} = 500$ nm, the normalized extent of three-phase boundary Λ is plotted as a function of the volume fraction φ_{el} for the three particle size ratios R considered. (b) Relative deviation between the measures Λ_{spc} and Λ_{line} as defined in Eq. (51) depending on the mean particle radius $\bar{r}$. The dashed line indicates that the radius of the smaller particle type goes below $r = 50$ nm.

where $\bar{r} = 500$ nm, and φ_{el}^{max} depends on the particle size ratio R. Fig. 5a shows the results as a function of φ_{el}, the volume fraction of electron conducting particles, while for all three binary particle mixtures considered the particle size ratio R and the particle radii r_{io} and r_{el} remain fixed. Note that results exist only for limited ranges of the volume fraction, φ_{el}, as outside those ranges either the electronic or the ionic particles fail to percolate. The case $R = 1$ represents the reference configuration as described in section 2.3.5, where the maximum for Λ occurs at $\varphi_{el}^{max} = \varphi_{io}^{max} = 0.5$. In this case, all three approaches coincide, thereby calibrating x_{inc} and x_{mat} in Eq. (13). For binary mixtures with different particle sizes, i.e. $R \neq 1$, the maximum in Λ for all three approaches shifts away from $\varphi_{el} = 0.5$: For $R > 1$, i.e. r_{io} is larger than r_{el}, the volume fraction of ion conducting particles has to be increased and that for electron conducting particles decreased in order to assure percolation, as previously reported [5,9,30]. The resulting maximum for Λ for $R = 4$ occurs at $\varphi_{el}^{max} = 0.228$ with $\varphi_{io}^{max} = 0.772$, and the particle sizes are $r_{el} = 151$ nm and $r_{io} = 604$ nm. When $R < 1$, the volume fraction of electronic particles must be increased and that for ionic particles decreased to assure percolation. As a result, the maximum for Λ for $R = 0.5$ occurs at $\varphi_{el}^{max} = 0.646$ with $\varphi_{io}^{max} = 0.354$, and the particle sizes are $r_{el} = 608$ nm and $r_{io} = 304$ nm. A significant difference becomes apparent from Fig. 5a when the extent of the TPB is compared for three mixtures of the same mean particle radius: While the maximum achievable values of Λ_{line} and Λ_{spc} show increases for $R \neq 1$ when compared to the reference configuration with $R = 1$, the maximum of Λ_{circ} for $R \neq 1$ drops below its reference value of $R = 1$. This finding is of importance, since it indicates that the approach of using Λ_{line} or Λ_{spc} will predict a behavior contrary to that found when Λ_{circ} is employed in a process for determining the best possible size ratio between electron and ion conducting particles in an anode or cathode.

For the three particle size ratios considered, Fig. 5b illustrates the relative deviation between the two TPB extents, Λ_{spc} and Λ_{line}, calculated as

$$\Delta_{spc,line} = \frac{(\Lambda_{spc}/\Lambda_{spc,0}) - (\Lambda_{line}/\Lambda_{line,0})}{(\Lambda_{line}/\Lambda_{line,0})} \quad (51)$$

as a function of the mean particle radius $\bar{r}$ of the binary mixture. For the reference configuration ($R = 1$, $\bar{r} = 500$ nm) Λ_{spc} and Λ_{line} concur as discussed before. The relative deviation, $\Delta_{spc,line}$, caused by taking spherical caps on the particles as electrochemically active surfaces instead of confining the electrochemical reactions to a one-dimensional line, amounts to 6.5% for $R = 0.5$ and 23% for $R = 4$ at a mean particle radius of $\bar{r} = 500$ nm. Lowering the mean particle radius leads to a (non-linear) increase of the relative deviations, indicating that Λ_{spc} grows faster than Λ_{line}.

In order to affirm the findings that Λ_{circ} shows considerably different results from Λ_{line} and Λ_{spc} when the extent of the TPB is calculated for a microstructure of particles of different size, Fig. 6 shows the normalized TPB extent as a function of the volume fraction φ_{el} and the particle size ratio R within a range from 1 to 10.

As before, the mean particle radius is kept constant at $\bar{r} = 500$ nm, so that according to Eqs. (48) and (49) the radii of the electric and ionic conducting particles become dependent on R and φ_{el} as

$$r_{el} = \frac{\bar{r}}{(1-\varphi_{el})R + \varphi_{el}} \text{ and } r_{io} = Rr_{el}. \quad (52)$$

Due to the fact that contact number conservation is fulfilled when the electron and ion conducting particles are interchanged (see section 2.2.4), Λ is unchanged under the transformation $R \rightarrow (1/R)$ and $\varphi_{el} \rightarrow (1 - \varphi_{el})$, so that it is sufficient to consider $R \geq 1$. Use of Λ_{spc} (Fig. 6a) and Λ_{line} (Fig. 6b) for the TPB extent shows similar behavior: the TPB extent increases when the particle size ratio R is raised and the mean particle radius is kept constant. However, the results diverge increasingly for high values of R: Since the mean particle size is fixed, the size of the electric conducting particle decreases for an increasing R and vice versa. In such circumstances the value of Λ_{spc} takes into account the fact that an increasing fraction of the smaller particle's surface becomes electrochemically active, a feature that is neglected in the case of Λ_{line}, causing the deviation.

In contrast, Λ_{circ} (Fig. 6c) exhibits a completely different dependence on R by showing a maximum for a mixture of equally sized particles with the same volume fraction. Changing the morphological parameters R and φ_{el} in this case always results in a decrease of the electrochemically active surface when compared to the reference configuration. A saddle-point value of $\Lambda_{circ} = 0.59$ $\Lambda_{circ,0}$ is reached at $R = 3.25$ for φ_{el} just greater than 0.2. Increasing

R further leads to a slight increase of Λ_{circ}, but even for unrealistically high values of R the reference value of $\Lambda_{circ,0}$ is not achieved.

As described in section 2.2.3 the calculation of Λ_{circ} is based on the assumption that the electrochemically active surface is proportional to the direct contact area between electron and ion conducting particles that is not accessible to the gas phase. Furthermore, experiments [21–23] indicate that the scaling behavior of the TPB extent for a monodisperse binary particle mixture follows $\Lambda \propto r^{-b}$, $b \approx 2$, instead of $b = 1$ as found for Λ_{circ}. Hence, we suggest that the approach of using Λ_{circ} for the TPB extent is not well suited for investigating binary mixtures of particles of different size. While the approaches of using Λ_{line} and Λ_{spc} agree with the experimentally observed scaling behavior, only Λ_{spc} allows for the electrochemical reaction to take place on the particles' surfaces, whereas Λ_{line} hypothetically confines the reaction to the one-dimensional contact perimeter line. Though both approaches coincide for binary mixtures of large, equally sized particles, this difference becomes increasingly important for binary mixtures containing particles of small size, i.e. when the electrochemical reaction takes place on a considerable portion of the smaller particle's surface. Then, the approach of using Λ_{spc} becomes physically more sound than use of Λ_{line} and we suppose that Λ_{spc} predicts the TPB extent more accurately. As a consequence, the electrochemically active three-phase boundary surface will be calculated from $\Lambda\Lambda_{spc}$ in the following, unless stated otherwise.

3.2. Parametric study of morphological parameters in anode and cathode

The microstructure's morphology in anode and cathode has a crucial impact on the fuel cell's performance. In the following, the influence of the electronic and ionic particle size, their size ratio and their volume fractions on the maximum achievable power density is investigated and ways are discussed for increasing the performance of the fuel cell. For this, the one-dimensional cell level model as described in section 2.3 is employed with all parameters as listed in Table 2. Typical operating conditions are chosen as boundary conditions, such as an operating temperature of $T = 1073$ K, a total gas pressure of 10^5Pa in both electrodes and fractional partial gas pressures at the inlet of $p^{ref}_{H_2} = 0.95$, $p^{ref}_{H_2O} = 0.05$ on the anode side (humified hydrogen) and $p^{ref}_{O_2} = 0.20$, $p^{ref}_{N_2} = 0.80$ on the cathode side (atmospheric oxygen

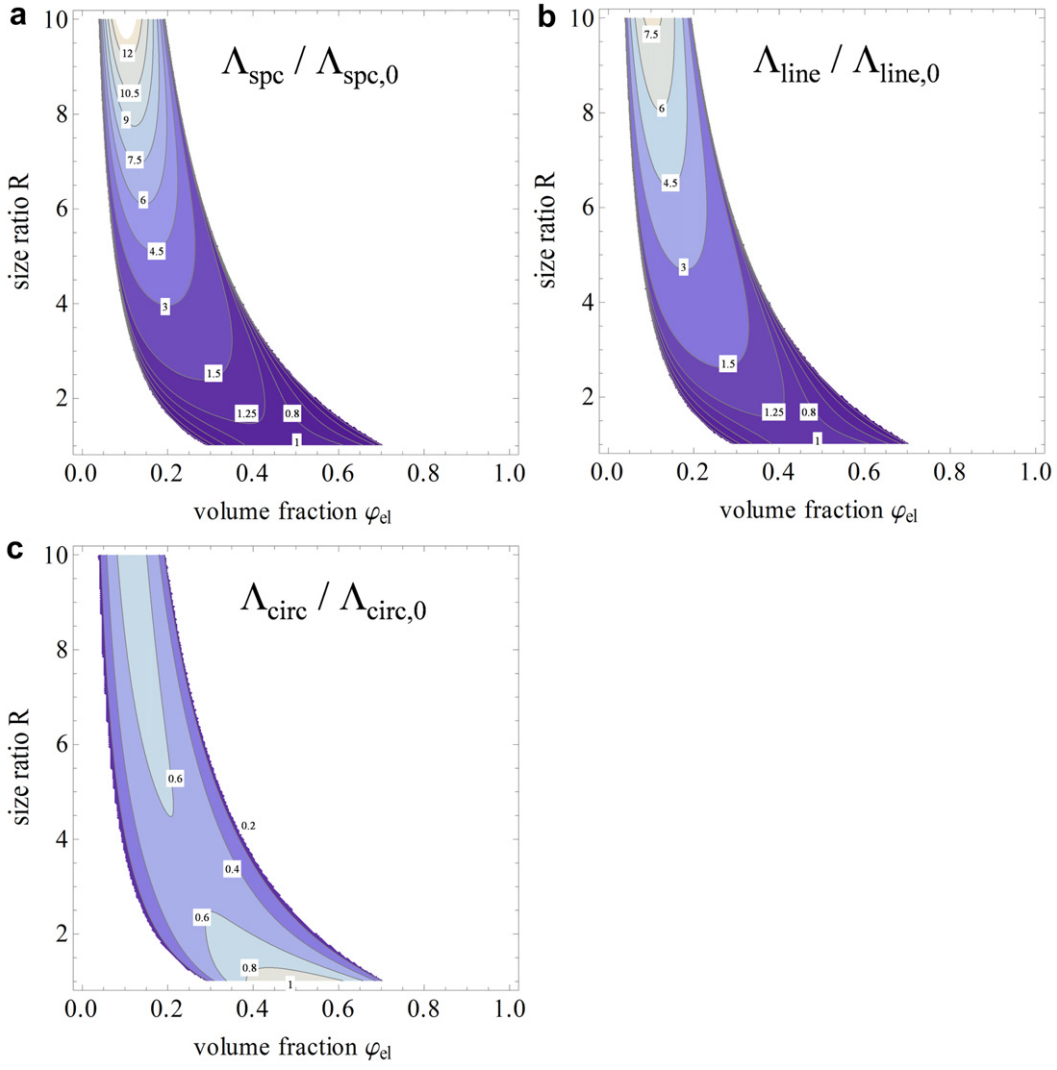

Fig. 6. Normalized three-phase boundary measures Λ_{spc}, Λ_{line} and Λ_{circ} depending on the particle size ratio R and volume fraction φ_{el} for binary mixtures of constant mean particle radius $\bar{r} = 500$ nm.

from air). This reference configuration shows a maximum achievable power density of $P_{max} = 16{,}490\ W\ m^{-2}$ at a cell voltage of $V_{op} = 0.49\ V$ and an operating current density of $i_{op} = 33{,}660\ A\ m^{-2}$.

3.2.1. Influence of particle size on performance

In order to investigate the influence of the particle size in anode and cathode, binary mixtures of electron and ion conducting particles of equal size ($R = 1$) with equal volume fractions $\varphi_{el} = \varphi_{io} = 0.5$ are considered. Results are shown as a function of particle size in Fig. 7a for the anode and in Fig. 7b for the cathode. Note that anode and cathode are examined separately: when properties on the anode side are considered, the microstructure parameters of the cathode are kept as those of the reference configuration and vice versa; recall that the reference configuration is a binary mixtures of electron and ion conducting particles with equal volume fractions $\varphi_{el} = \varphi_{io} = 0.5$ and equal particle size ($R = 1$) of $r_{io} = r_{el} = 500$ nm. It can be seen in Fig. 7 that the power density is maximized at a finite particle size. On the anode side, when $\Lambda = \Lambda_{spc}$, the maximum power density occurs for particles of radius $r_{el} = r_{io} = 435$ nm and is $P^{0,an}_{max} = 16{,}530\ W\ m^{-2}$, a small increase of 0.2% over the reference configuration in which $r_{el} = r_{io} = 500$ nm and $P_{max} = 16{,}490\ W\ m^{-2}$. Monodisperse anodes with particle radii between approximately 300 nm and 500 nm show almost the same performance. When the particle size in a monodisperse cathode is varied, a maximum power density of $P^{0,ca}_{max} = 21{,}410\ W\ m^{-2}$ is achieved for $r_{el} r_{io} = 150$ nm for $\Lambda = \Lambda_{spc}$, representing an increase of 30% compared to the reference configuration in which $r_{el} = r_{io} = 500$ nm and the power density is $P_{max} = 16{,}490\ W\ m^{-2}$. In contrast to the anode, the maximum occurs for relatively small particles and is fairly sharp. The maximum achievable power densities $P^{0,an}_{max}$ and $P^{0,ca}_{max}$ for monodisperse electrodes of equal volume fraction $\varphi_{el} = \varphi_{io} = 0.5$ will be used as reference values for further parametric studies on the particle size ratio R and the volume fractions φ_{el}&φ_{io}. Note that all results are given and compared for all three models Λ_{circ}, Λ_{line} and Λ_{spc} for the extent of the TPB in Fig. 7a and b. As expected, the results for both Λ_{line} and Λ_{spc} are qualitatively similar, whereas the results for Λ_{circ} deviate significantly.

3.2.2. Influence of volume fractions

For electrodes consisting of a binary mixture of monodisperse particles, the volume fractions of electron and ion conducting particles have an effect on the cell's performance. In Fig. 8 the maximum achievable power density as a function of the particle size is compared for two cases: in the reference case, the volume fractions of electron and ion conducting particles are chosen to be identical so that $\varphi_{el} = \varphi_{io} = 0.5$. In the other case, the volume fractions φ_{el} and $\varphi_{io} = 1 - \varphi_{el}$ are varied within the percolation limits for a given particle size until the largest possible power density is obtained. All computations in this case are carried out with $\Lambda = \Lambda_{spc}$. Fig. 8 shows the volume fraction, φ_{el}, yielding the highest power density, as well as the resulting value of the power density.

Considering the anode (Fig. 8a), we find that the volume fraction yielding the highest power density is approximately $\varphi_{el} = 0.5$ for small particles having $r = 200$ nm, decreasing to $\varphi_{el} = 0.44$ for $r = 1000$ nm. In contrast, for the cathode electrode (Fig. 8b) a constant volume fraction of $\varphi_{el} = 0.415$ yields the highest power density within the range of $r = 200$ nm to $r = 1000$ nm, dropping to smaller volume fractions only for particles smaller than this range. Since the volume fractions in monodisperse particle mixtures influence the available TPB as well as the ionic and electronic conductivities in the electrode, but not the pore radius, the volume fractions giving the maximum power density represent a trade-off between activation and Ohmic losses, and depend on design parameters (e.g. thickness of the electrode) as well as material parameters (e.g. bulk conductivities of the electronic and ionic conducting phases). For our specific model, the power density can be increased by 1% ($r = 1000$ nm) in the anode and by 4% ($r = 1000$ nm) in the cathode when compared to electrodes with identical volume fractions. When compared to the values of $P^{0,an}_{max}$ and $P^{0,ca}_{max}$ found in section 3.2.1 for the particle sizes that yield the highest power density, further performance gains of approx. 0.3% ($r = 435$ nm, $\varphi_{el} = 0.46$) for the anode and 2% ($r = 150$ nm, $\varphi_{el} = 0.415$) for the cathode can be achieved by varying the volume fractions within the percolation limits. The benefit of varying the volume fractions away from $\varphi_{el} = \varphi_{io} = 0.5$ are thus seen to be modest, even negligible.

3.2.3. Influence of size ratio and volume fractions

Up to this point, only monodisperse particle mixtures with electron and ion conducting particles of equal size have been considered. However, the particle size ratio, R, between electron and ion conducting particles, as defined in Eq. (48), influences also the effective material properties and thus the cell's performance.

In order to quantify this influence, Fig. 9 illustrates the effect of differently sized electronic and ionic particles on the power density.

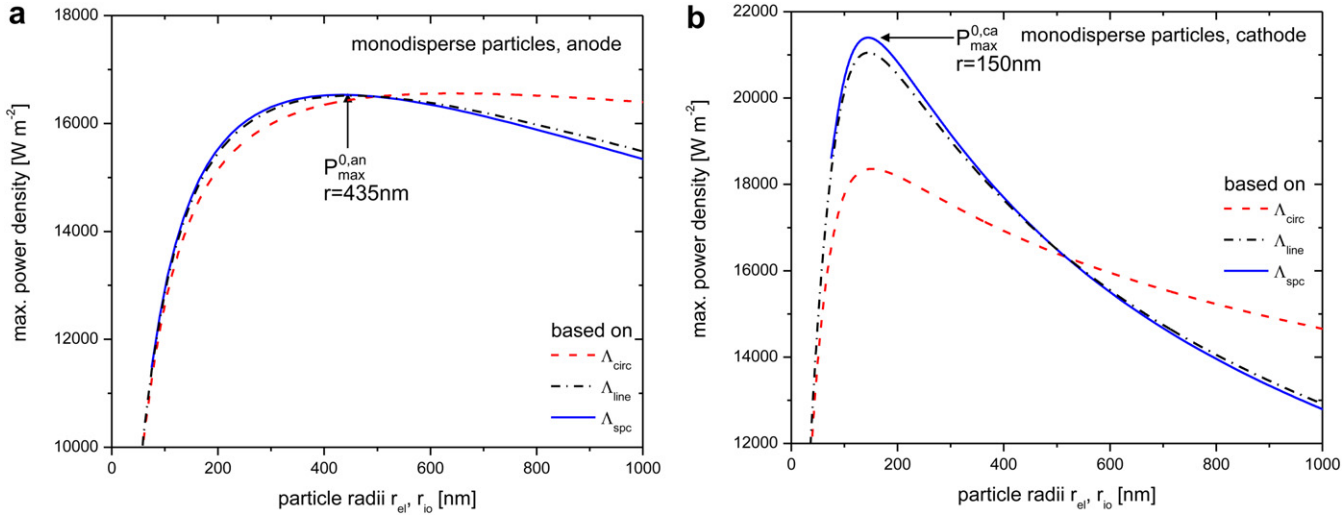

Fig. 7. Influence of the particle size in monodisperse particle mixtures ($r_{io} = r_{el}$) with identical volume fractions $\varphi_{io} = \varphi_{el} = 0.5$ on the maximum achievable power density.

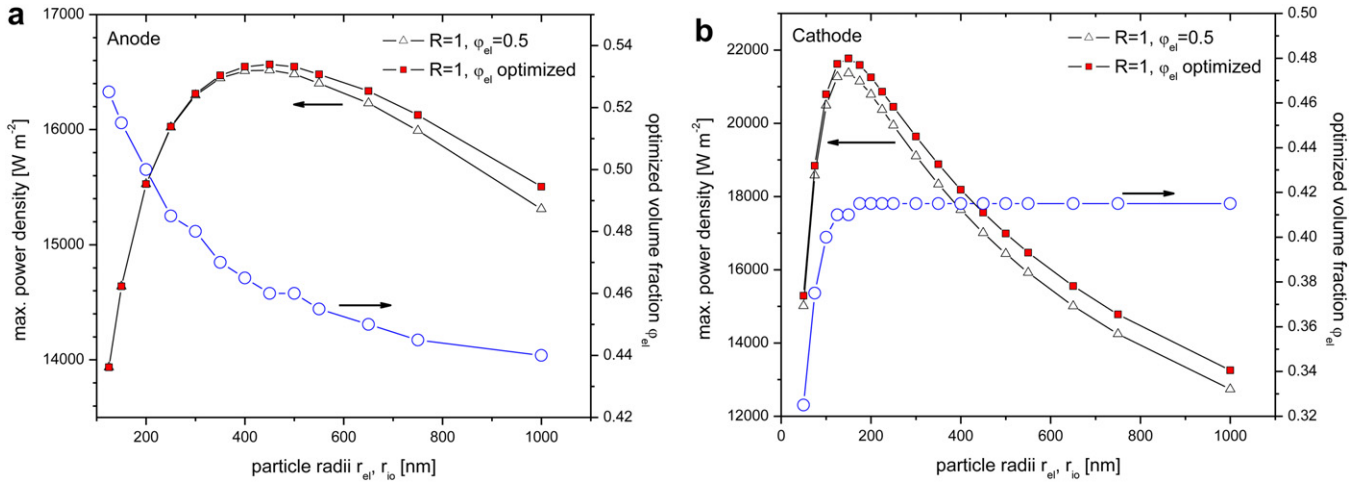

Fig. 8. Influence of the volume fraction φ_{el} for electrodes consisting of monosized particles ($R = 1$) on the maximum achievable power density.

For various fixed values of the radius of the ion conducting particle, r_{io}, the maximum achievable power density is shown as a function of the radius of the electron conducting particle r_{el}. For that purpose, for every combination of r_{el} and r_{io} the volume fraction, φ_{el}, which yields the highest power density, is determined in a series of calculations. For better comparability, the maximum power densities are normalized by $P^{0,an}_{max}$ and $P^{0,ca}_{max}$ (see section 3.2.1) and results for monodisperse particles ($R = 1$) with equal volume fractions ($\varphi_{el} = \varphi_{io} = 0.5$) are plotted in addition. Such calculations are carried out for both anodes and cathodes with electronic particle radii ranging between $r_{el} = 25$ nm and $r_{el} = 1000$ nm, with the restriction that $r_{io} \geq 25$ nm, and volume fractions ranging between $\varphi_{el}^{perc,low} \leq \varphi_{el} \leq \varphi_{el}^{perc,up}$, where $\varphi_{el}^{perc,low}$ and $\varphi_{el}^{perc,up}$ represent the lower and upper percolation limit for electron conducting particles. This study shows that for the anode (Fig. 9a) as well as for the cathode (Fig. 9b) particle mixtures of differently sized electric and ionic particles, i.e. $R \neq 1$,lead to increased power densities when compared to mixtures of monodisperse particles with equal volume fractions.

Furthermore, a simultaneous parametric study of the particle size ratio R and the volume fraction φ_{el} is performed: for fixed radii of the electron conducting particle r_{el}, the particle size ratio R and volume fraction φ_{el} are varied until for each combination of r_{el}, R and φ_{el} the maximum achievable power density is determined using $\Lambda = \Lambda_{spc}$. This is exemplified by Fig. 10 for a cathode with $r_{el} = 75$ nm: in this case the highest power density is achieved for a size ratio of $R = 4.7$ and an electric particle volume fraction of $\varphi_{el} = 0.16$, resulting in a power density of 23,610 W m^{-2}. The results of the simultaneous parametric study on particle size ratio R and volume fraction φ_{el}, showing their influence on the maximum achievable power density, are illustrated in Fig. 11. As a function of the size of the electron conducting particle, it shows the maximum power density that can be obtained when the particle size ratio R and volume fraction φ_{el} are varied simultaneously. In this study, we impose restrictions on the minimum particle size (r_{el}, $r_{io} \geq 50$ nm) and the particle size ratio ($1/10 \leq R \leq 10$). As before, the maximum power densities are normalized by $P^{0,an}_{max}$ and $P^{0,ca}_{max}$ and results for monodisperse particles ($R = 1$) with equal volume fractions ($\varphi_{el} = \varphi_{io} = 0.5$) are plotted as comparison.

When considering the anode (Fig. 9a and 11a), we find that for electron conducting particle sizes smaller than $r_{el} = 450$ nm

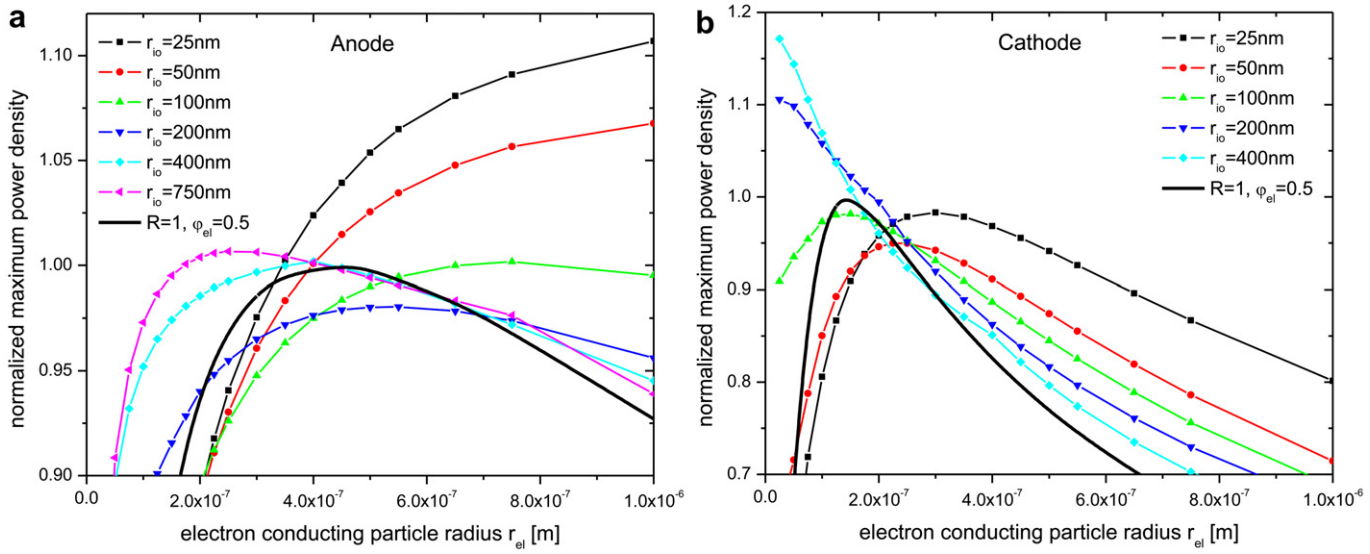

Fig. 9. For various fixed values of the ionic particle size, r_{io}, the maximum achievable power densities in anode (a) and cathode (b) are plotted as a function of the electronic particle size, r_{el}. For each combination of r_{el} and r_{io} the volume fraction φ_{el} is varied within the percolation limits until the highest power density is identified. The power densities are normalized by $P^{0,an}_{max}$ and $P^{0,ca}_{max}$ as determined in Fig. 7.

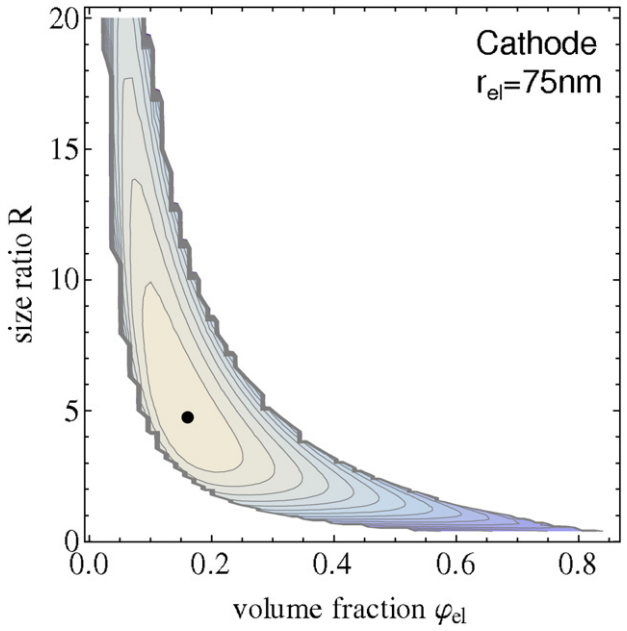

Fig. 10. The maximum achievable power density of a cathode with $r_{el} = 75$ nm as a function of the particle size ratio R and the volume fraction φ_{el}. A maximum is reached for $R = 4.7$ and $\varphi_{el} = 0.16$, indicated by the spot.

a particle size ratio of $R > 1$ becomes favorable, leading to significant performance increases when compared to the reference case of monodisperse particles. However, when compared to $P^{0.an}_{max}$, arising from $R = 1$ and $\varphi_{el} = \varphi_{io} = 0.5$ with $r_{el} = r_{io} = 435$ nm, only a very small performance gain of about 0.7% (at $r_{el} = 250$ nm, $R = 3.2$, $\varphi_{el} = 0.27$) is found. For electronic particle sizes larger than $r_{el} = 450$ nm, the simulations indicate that particle mixtures of small particle size ratio ($R < 0.2$) become favorable and lead to an increased performance. For example, for a mixture of $r_{el} = 600$ nm, $r_{io} = 60$ nm and $\varphi_{el} = 0.93$, a performance gain of 3% compared to $P^{0.an}_{max}$ is found. This performance gain becomes even larger when smaller ionic particle sizes or smaller particle size ratios are permitted.

When considering the cathode (Fig. 9b and 11b), we find that for electron conducting particle sizes smaller than $r_{el} = 200$ nm, a particle size ratio of $R > 1$ leads to an increase of the maximum achievable power density. For example, for a binary particle mixture of $r_{el} = 50$ nm, $r_{io} = 420$ nm ($R = 8.4$) and $\varphi_{el} = 0.1$, a 14.4% gain of the power density is found compared to $P^{0.ca}_{max}$, arising from $R = 1$ and $\varphi_{el} = \varphi_{io} = 0.5$ with $r_{el} = r_{io} = 150$ nm. This performance gain becomes even larger when smaller electronic particle sizes or larger particle size ratios are permitted. In a size range for the electronic particle between 200 nm $< r_{el} <$ 250 nm, the maximum of the power density is found for monodisperse particle mixtures ($R = 1$) where only the volume fractions are varied away from $\varphi_{el} = \varphi_{io} = 0.5$ (as described in section 3.2.2). Then, for electronic particle sizes larger than $r_{el} = 250$ nm, binary mixtures with particle size ratios of $R < 1$ become favorable when compared to the monodisperse reference configuration with equal particle sizes and volume fractions. In contrast to our results for the anode, we find it not possible to increase the maximum achievable power density compared to $P^{0.ca}_{max}$ for electronic particle sizes of $r_{el} > 200$ nm when we simultaneously vary the particle size ratio and the volume fractions within the described ranges, even for particle mixtures of very small particle ratio and ionic particle radii as small as $r_{io} = 25$ nm. In summary, when compared to monodisperse electrodes with electron and ion conducting particles of same size, our model predicts an increased performance of electrodes with electron and ion conducting particles of different size (i.e. $R \neq 1$) over a wide range of particle sizes.

3.2.4. Discussion of the parametric study

In order to interpret the results of the parametric study, and for better understanding, the dependence of the effective material parameters (three-phase boundary extent Λ, electric conductivity σ^{eff}_{el}, ionic conductivity σ^{eff}_{io}, effective pore radius r_{pore}) upon the particle size ratio R and the volume fraction φ_{el} for a fixed electric particle size r_{el} is plotted qualitatively in Fig. 12. Arrows indicate the direction in which the respective parameters increase.

When the size of the electron conducting particle r_{el} is kept constant, the extent of the TPB increases for small particle size ratios, i.e. $r_{io} < r_{el}$, and high volume fractions, φ_{el}, ensuring percolation, a trend that occurs due to an increase in the number of ion

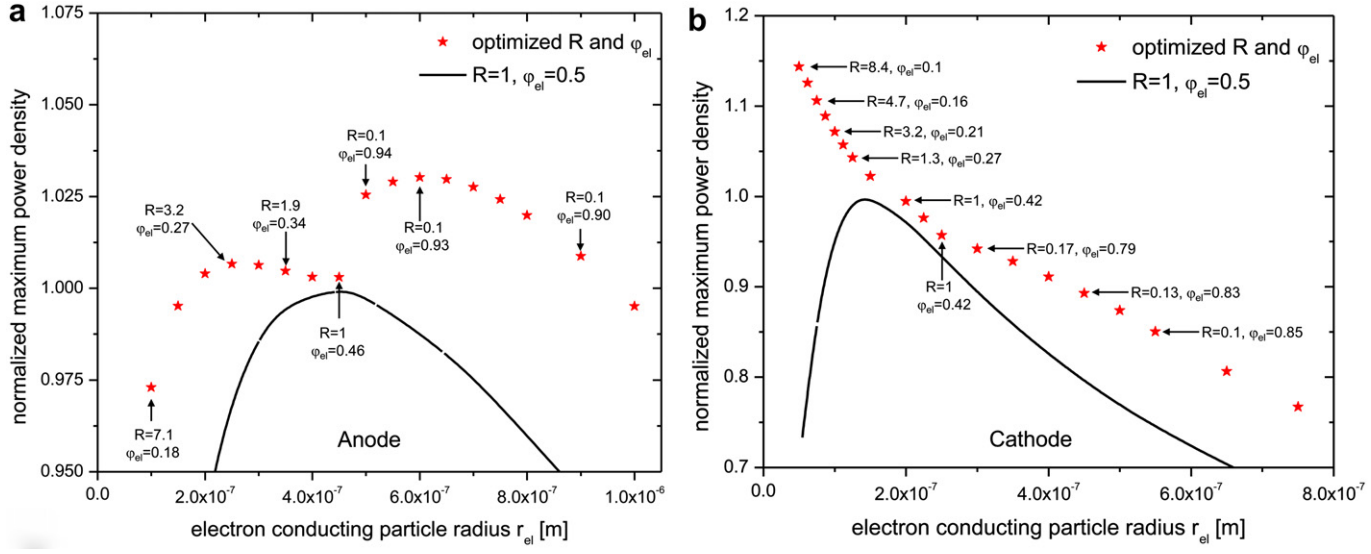

Fig. 11. Maximum achievable power density in anode (a) and cathode (b) for a simultaneous variation of the particle size ratio R and the volume fraction φ_{el} as a function of the electronic particle radius r_{el}. Restrictions on the minimum particle size (r_{el},$r_{io} \geq 50$ nm) and the particle size ratio ($1/10 \leq R \leq 10$) are imposed. The maximum power densities are normalized by $P^{0.an}_{max}$ and $P^{0.ca}_{max}$ as determined in Fig. 7.

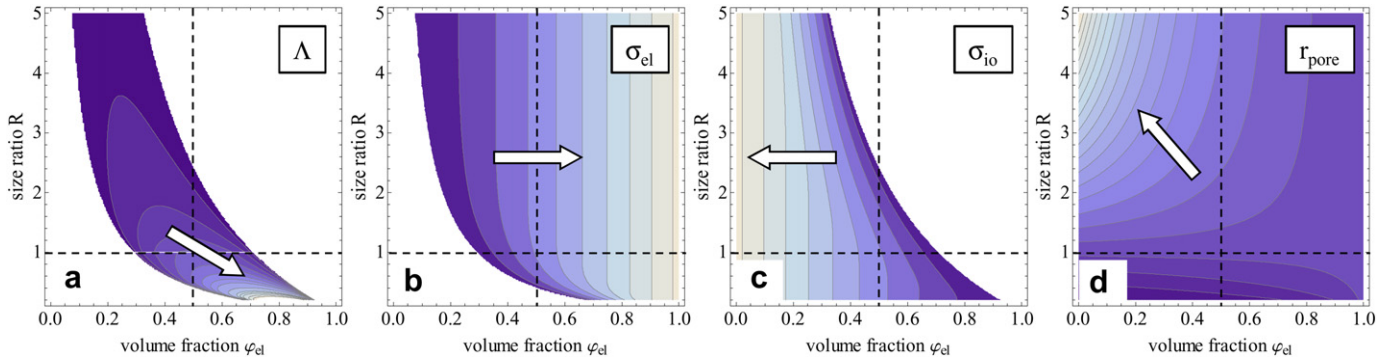

Fig. 12. Material parameters qualitatively depending on particle size ratio R and volume fraction φ_{el} for r_{el} kept constant: three-phase boundary Λ, conductivities σ_{el}, σ_{io} and pore radius r_{pore}. Arrows indicate in which direction the respective properties increase.

conducting particles and therefore of the electrochemically active contacts. The direction in which Λ increases in Fig. 12a is therefore down and to the right as indicated by the arrow. In contrast, the pore radius increases for large size ratio, R, and small particle volume fraction, φ_{el}, leading to a smaller resistance in the gas flow and therefore to smaller concentration losses when the particle size ratio is increased. This trend is apparent in Fig. 12d. This means that when the size ratio is changed in order to decrease activation losses by increase of Λ, the concentration losses are inevitably increased and vice versa. The ion and electron conductivities mainly depend on the volume fractions of the respective phases, so that an increase of one conductivity directly causes a decrease of the other, characterized by the opposite trends in Fig. 12b and d. Thus, a best possible performance is only achieved when the overall effect of activation losses, Ohmic losses and concentration losses is minimized, trading off the disparate trends in Fig. 12.

As presented in section 3.2.1, our model utilizing the new three-phase boundary approach characterized by Λ_{spc} predicts that for electrodes consisting of a monodisperse ($R = 1$) binary particle mixture with identical volume fractions ($\varphi_{el} = 0.5$), a maximum in power density and thus in performance is reached for a well-defined finite particle size, which is in agreement with previous studies [6,13]. A further improvement of the electrode's performance can be achieved by subsequently varying the volume fractions of the electron and ion conducting phases within the percolation limits, as discussed in section 3.2.2, tending to shift the volume fraction of the electron conducting phase to values below $\varphi_{el} = 0.5$, i.e. increasing the volume fraction of the ion conducting phase, and therefore increasing the effective ionic conductivity. This can be explained by the difference between the ionic and electronic bulk conductivities, which involves several orders of magnitude (see Eqs. (45)–(47)). Thus, the overall Ohmic losses can be reduced by increasing the ionic conductivity without much penalty arising from the accompanying decrease in the electronic conductivity. However, a decreasing φ_{el} also reduces Λ, so that a trade-off between activation and Ohmic losses must be found. Chan et al. [30] reported similar findings from use of a cathode micro-model. They conclude that a minimum of the overall losses and thus a maximum in performance can be achieved for $R = 1$ and $\varphi_{io} = 0.6$. In this work, we show that the ideal volume fraction leading to maximum performance is not independent of the particle size in the electrodes: when evaluating the functional dependency of the volume fraction φ_{el} on the maximum achievable power density in an anode, we find that the volume fraction φ_{el} that maximizes the power density increases with decreasing particle radius, whereas the respective volume fraction φ_{el} that maximizes the power density in a cathode decreases with decreasing particle radius. This opposite trend is a consequence of the different thickness of anode and cathode as well as the different expansion of the reaction zones in anode and cathode.

Several previous theoretical studies on the impact of the particle size ratio R on an electrode's performance stated that a particle size ratio of $R = 1$, i.e. electron and ion conducting particles of the same size, should be chosen in order to achieve the maximum performance of the electrode in terms of power density [6,17,30,31]. Contrary to these studies, our findings shown in section 3.2.3 indicate that the performance of anode and cathode can be further enhanced by varying the particle size ratio away from $R = 1$, and enhancements in the power density for $R \neq 1$ are found.

When the performance of electrodes that consist of differently sized particle types, i.e. $R \neq 1$, is investigated, the approach for calculating the effective three-phase boundary is crucial, as discussed earlier in section 3.1. For those studies employing a TPB approach in which Λ_{circ} characterizes its extent [5,6], a particle size ratio $R \neq 1$ always results in a decrease of Λ, so that such studies will predict an ideal particle size ratio of $R = 1$, regardless of the particle sizes and volume fractions. Other studies on the influence of the particle size ratio used a TPB approach in which Λ_{line} characterizes its extent [17,30,31], and exhibit the experimentally observed scaling behavior (cf. section 3.1).

For example, in a parameter study for a cathode, Chen et al. [17] considered a constant volume fraction φ_{el} when investigating the impact of the particle size ratio R, hence finding minimal losses in the cathode for $R = 1$. However, as shown in our work, a variation of R always has to be accomplished by a simultaneous variation of the volume fractions φ_{el} and $\varphi_{io} = 1 - \varphi_{el}$ in order to enhance the power density. While Chan et al. [30] and Chen et al. [31] took the influence of φ_{el} into account, they only considered a few specific combinations of r_{el} and R, from which they concluded that an ideal value is $R = 1$. Furthermore, in all studies previously mentioned only the electrode's performance for a specific current density was considered.

In contrast, we have systematically investigated the performance of anode and cathode, accounting for a large range of particle size ratios, volume fractions φ_{el} and particle radii. Our model, employing the new three-phase boundary approach in which Λ_{spc} characterizes its extent, predicts that the performance of composite cathodes can be enhanced when electron conducting particles with $r_{el} < 200$ nm and bigger ion conducting particles are used, i.e. a particle size ratio $R > 1$, instead of monodisperse particles. In anodes, significant enhancements are only possible for rather small particle size ratios ($R < 0.2$).

In Fig. 13a and b, cell voltage and power density characteristics of anodes and cathodes are plotted as functions of the current density, with morphological parameters that yield highest performance in the examined ranges of particle sizes and volume

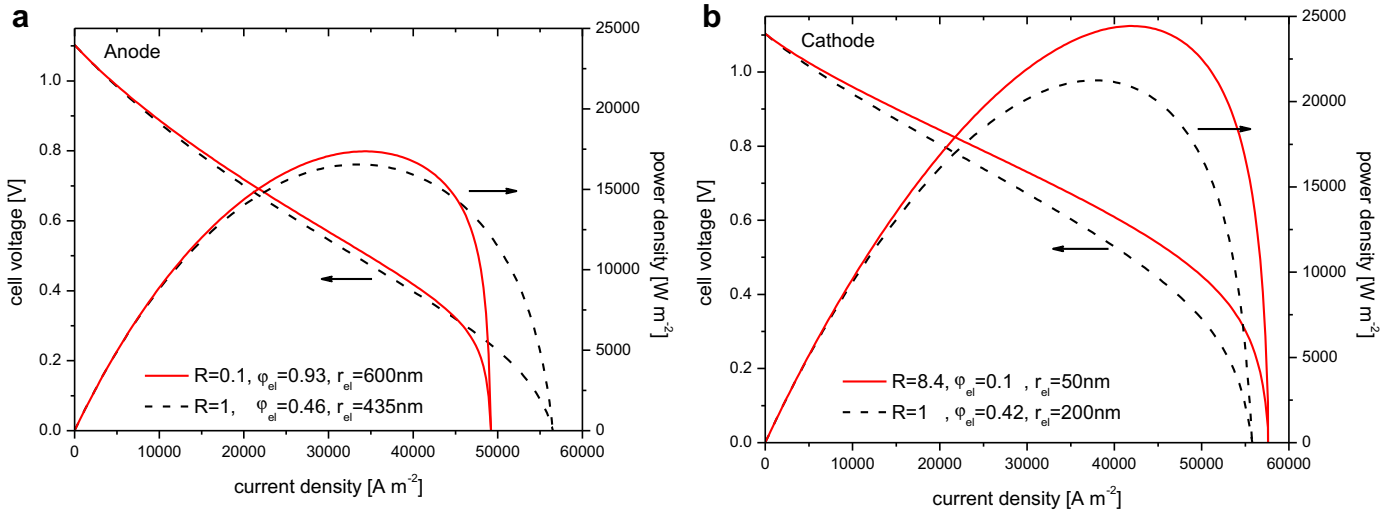

Fig. 13. Cell voltage and power density depending on the current density for anode and cathode microstructures with morphological parameters that yield the highest power densities as identified in the parametric study. Solid line: Parameters yielding the maximum power density when particle size and volume fraction are modified simultaneously. Dashed line: Parameters yielding the maximum power density when only the volume fractions are varied, but not the particle size ratio so that $R = 1$.

fractions as identified in the parametric study. Two cases are considered: anodes and cathodes with parameters yielding the maximum power density when particle size ratio, particle size and volume fraction are varied simultaneously (solid lines), and for comparison, anodes and cathodes with parameters yielding the maximum power density when only the volume fractions are varied (cf. section 3.2.2), but not the particle size ratio so that $R = 1$ (dashed lines). A restriction to the minimum particle size, r_{el},$r_{io} \geq 50$ nm, as well as to the particle size ratio, $0.1 \leq R \leq 10$, has been imposed.

For the anode, our simultaneous parametric study of particle size ratio, particle size and volume fraction in the described ranges identified a particle size ratio $R = 0.1$ and a volume fraction of the electron conducting particles, $\varphi_{el} = 0.93$, as the morphological parameters that yield the highest achievable power density. This small particle size ratio of $R = 0.1$ and the high volume fraction of electron conducting particles, $\varphi_{el} = 0.93$, lead to a reduced ionic conductivity and a smaller mean pore radius when compared to the best configuration with equally sized particles, having $r_{io} = r_{el} = 435$ nm ($R = 1$) and a volume fraction of the electric phase of $\varphi_{el} = 0.46$. In Fig. 13a this becomes apparent from the steeper decrease of both the cell voltage and the power density for high current densities, and a reduced maximum current density, indicating higher concentration losses. This is compensated by a strongly increased extent of the TPB and an increased electronic conductivity (cf. Fig. 12), leading to an overall increase of the maximum achievable power density. For the anode-supported SOFC design considered, variation of the particle size ratio away from $R = 1$ yields enhancements of the power density only for particle size ratios above a threshold of $R < 0.2$, while within $0.2 \leq R \leq 1$ it does not lead to an improved performance. Note that the small particle size ratio necessary might already approach the limits of reliability of percolation theory [36,45], so that we suggest that varying the particle size ratio away from $R = 1$ in order to increase the power density is only of limited value.

For the cathode, our simultaneous parametric study of particle size ratio, particle size and volume fraction in the described ranges identified a particle size ratio $R = 8.4$ and a volume fraction of the electron conducting particles $\varphi_{el} = 0.1$ as the morphological parameters that yield the highest achievable power density. This high particle size ratio of $R = 8.4$ and the low volume fraction of the electron conducting particles, $\varphi_{el} = 0.1$, lead to an increased ionic conductivity, a larger mean pore radius and an increased extent of TPB when compared to the configuration with equally sized particles of $r_{el} = 200$ nm and a volume fraction of the electric phase of $\varphi_{el} = 0.42$, where only the particle sizes and volume fractions were varied in the respective parametric study for identifying the highest achievable power density, while the particle size ratio was kept at $R = 1$. In Fig. 13b this becomes apparent from the increased maximum current density and from the decreased slope of the cell voltage, indicating reduced activation, concentration and Ohmic losses when compared to a mixture of monodisperse particles. In contrast to the aforementioned anode, our parametric study indicates that a variation of the particle size ratio away from $R = 1$ yields enhancements of the power density monotonically for $R > 1$ and is only limited by the size of the smaller particle r_{el} in the binary mixture. Hence, we suggest that for certain design parameters the particle size ratio R can be used to improve the performance of composite cathodes, when the volume fractions are varied simultaneously.

4. Conclusion

In this work a new approach for calculating the effective three-phase boundary extent in porous anodes and cathodes of SOFCs is proposed. The new approach is motivated by the assumption that the electrochemical reaction takes place on the surfaces of contacting electron and ion conducting particles within a certain width of the contact perimeter. This is in contrast to prior approaches, which either assume that the reactive site is the contact area between electron and ion conducting particles or confine the electrochemical reaction to the one-dimensional contact perimeter line. Hence, the new approach is physically more sound. The approach introduced is compared to previous ones found in the literature, and its advantages for calculating effective properties of binary particle electrodes with particles of different size are shown.

Furthermore, the new approach for calculating the effective three-phase boundary extent is employed in a parametric study, investigating the influence of the morphological parameters of porous anode and cathode microstructures on their performance. For electrodes consisting of a binary mixture of spherical electron and ion conducting particles, the influence of the particle size, the

particle size ratio and the volume fractions on the cell's performance is investigated by use of a one-dimensional cell level model accounting for the processes of gas transport, electron and ion conduction as well as the electrochemical reactions. Based on this study, we suggest that under certain conditions the performance of cathodes can be enhanced by choosing a microstructure with electronic conducting particles of size different from that of the ionic conducting particles when compared to the best possible configuration of monodisperse particles.

Acknowledgments

The authors gratefully acknowledge the financial support by the Energy Frontiers Research Center on Physics Based Nano-Structure Design and Synthesis of Heterogeneous Functional Materials for Energy Systems (HeteroFoaM) funded by the U.S. Department of Energy. We acknowledge support from the Center for Scientific Computing at the CNSI and MRL: an NSF MRSEC (DMR-1121053) and NSF CNS-0960316.

Nomenclature

A	area [m^2]
D	diffusivity [$m^2\ s^{-1}$]
E_{H_2}	activation energy for H_2 oxidation [J mol^{-1}]
E_{O_2}	activation energy for O_2 reduction [J mol^{-1}]
E^{eq}	equilibrium electric potential difference at reaction interface [V]
F	Faraday's constant, 96,485 [C mol^{-1}]
G_α	Gibbs free energy of species α [J mol^{-1}]
i	electrochemical reaction current density [A m^{-2}]
i^0	reference exchange current density [A m^{-2}]
i_{op}	operating current density [A m^{-2}]
k	thermal conductivity [W $m^{-1}\ K^{-1}$]
L	length [m]
n_k	number of k-particles per unit volume
N_α	molar flux of species α [mol $m^{-2}\ s^{-1}$]
N_A	Avogadro's constant, 6.02210^{-23} [mol^{-1}]
M_α	molecular weight of species α [kg mol^{-1}]
p_α	partial pressure of gas species α [Pa]
p_0	total pressure [Pa]
P_k	percolation probability of k-particle
r_{pore}	mean hydraulic pore radius [m]
r_k	radius of k-particle [m]
R	diameter ratio of particles
$\bar{R}$	universal gas constant, 8314 [J $mol^{-1}\ K^{-1}$]
Q	heat source [W m^{-2}]
T	temperature [K]
V_{op}	operating cell voltage [V]
z	moles of electrons per mole of reactant
Z_0	overall average coordination number of all solid particles
Z_k	average coordination number of k-particle
Z_{k-1}	average number of contacts between k-particles and l-particles

Greek

α	amount of reactive sites per contact pair, [m] or[m^2]
β	charge transfer constant
γ	reference exchange current factor
ε	porosity
η	activation overpotential [V]
Γ_α	collision diameter of species α [m]
Λ	effective three-phase boundary (TPB) in [m^{-2}] or [m^{-1}]
Λ_{circ}	extent of TPB based on approach in Eq. (11) [m^{-1}]
Λ_{line}	extent of TPB based on approach in Eq. (12) [m^{-2}]
Λ_{spc}	extent of TPB based on approach in Eq. (2.2.3) [m^{-1}]
μ	Bruggeman factor
φ_k	volume fraction k-type particles, relative to solid material
Φ	electric potential [V]
ρ	resistivity [Ω m]
σ	conductivity [$\Omega^{-1}\ m^{-1}$]
τ	tortuosity
θ	contact angle between electrode- and electrolyte particles
$\Omega_{\alpha\beta}$	collision integral for species α and β

Subscripts

el	electronic
io	ionic
an	anode
ca	cathode
lyte	dense electrolyte
joule	joule heating
conc	concentration
act	activation
K	Knudsen

Superscripts

eff	effective
ref	reference
TPB	three-phase boundary

Appendix A. Supplementary material

Supplementary material associated with this article can be found, in the online version, at doi:10.1016/j.jpowsour.2012.05.014.

References

[1] B. Kenney, M. Valdmanis, C. Baker, J.G. Pharoah, K. Karan, J. Power Sources 189 (2009) 1051–1059.
[2] C. Metcalfe, O. Kesler, T. Rivard, F. Gitzhofer, N. Abatzoglou, J. Electrochem. Soc. 157 (9) (2010) B1326–B1335.
[3] Q. Cai, C.S. Adjiman, N.P. Brandon, Electrochim. Acta 56 (2011) 5804–5814.
[4] Q. Cai, C.S. Adjiman, N.P. Brandon, Electrochim. Acta 56 (2011) 10809–10819.
[5] P. Costamagna, P. Costa, V. Antonucci, Electrochim. Acta 43 (1998) 375–394.
[6] S.H. Chan, Z.T. Xia, J. Electrochem. Soc. 148 (4) (2001) A388–A394.
[7] D.H. Jeon, J.H. Nam, C.-J. Kim, J. Electrochem. Soc. 153 (2) (2006) A406–A417.
[8] M. Ni, M.K. Leung, D.Y.C. Leung, Chem. Eng. Technol. 5 (2007) 587–592.
[9] D. Chen, Z. Li, H. Zhu, R.J. Kee, J. Power Sources 191 (2009) 240–252.
[10] P. Chinda, W. Wechsatol, S. Chanchaona, P. Brault, Fuel Cells 2 (2011) 184–199.
[11] J. Shi, X. Xue, J. Fuel Cell Sci. Technol. 8 (2011) 011005–11011–10.
[12] P. Costamagna, A. Selimovic, A.D. Borghi, G. Agnew, Chem. Eng. J. 102 (2004) 61–69.
[13] M. Cannarozzo, S. Grozzo, G. Agnew, A.D. Borghi, P. Costamagna, J. Fuel Cell Sci. Technol. 4 (2007) 99–106.
[14] S. Sunde, J. Electroceram. 5 (2) (2000) 153–182.
[15] A. Abbaspour, X. Wen, K. Nandakumar, J. Luo, K.T. Chuang, J. Power Sources 185 (2008) 961–966.
[16] V.M. Janardhanan, V. Heuveline, O. Deutschmann, J. Power Sources 178 (2008) 362–372.
[17] D. Chen, W. Bi, W. Kong, Z. Lin, J. Power Sources 195 (2010) 6598–6610.
[18] H. Iwai, N. Shikazono, T. Matsui, H. Teshima, M. Kishimoto, R. Kishida, D. Hayashi, K. Matsuzaki, D. Kanno, M. Saito, H. Muroyama, K. Eguchi, N. Kasagi, H. Yoshida, J. Power Sources 195 (4) (2010) 955–961.
[19] J.R. Wilson, W. Kobsiriphat, R. Mendoza, H.-Y. Chen, J.M. Hiller, D.J. Miller, K. Thornton, P.W. Voorhees, S.B. Adler, S.A. Barnett, Nat. Mater. 5 (7) (2006) 541–544.
[20] J.R. Wilson, J.S. Cronin, A.T. Duong, S. Rukes, H.-Y. Chen, K. Thornton, D.R. Mumm, S.A. Barnett, J. Power Sources 195 (7) (2010) 1829–1840.
[21] S.-D. Kim, H. Moon, S.-H. Hyun, J. Moon, J. Kim, H.-W. Lee, J. Power Sources 163 (2006) 392–397.
[22] J. Chen, F. Liang, L. Liu, S. Jiang, B. Chi, J. Pu, J. Li, J. Power Sources 183 (2008) 586–589.
[23] Z. Jiang, L. Zhang, K. Feng, C. Xia, J. Power Sources 185 (2008) 40–48.
[24] M. Shiskin, T. Ziegler, J. Phys. Chem. C 114 (2010) 11209–11214.
[25] M. Vogler, A. Bieberle-Hütter, L. Gauckler, J. Warnatz, W.G. Bessler, J. Electrochem. Soc. 156 (5) (2009) B663–B672.

[26] D.G. Goodwin, H. Zhu, A.M. Colclasure, R.J. Kee, J. Electrochem. Soc. 156 (9) (2009) B1004–B1021.
[27] K.N. Grew, A.S. Joshi, A.A. Peracchio, W.K.S. Chiu, J. Power Sources 195 (2010) 2331–2345.
[28] Y. Jiang, A.V. Virkar, J. Electrochem. Soc. 150 (7) (2003) A942–A951.
[29] M.M. Hussain, X. Li, I. Dincer, J. Power Sources 161 (2006) 1012–1022.
[30] S.H. Chan, X.J. Chen, K.A. Khor, J. Electrochem. Soc. 151 (1) (2004) A164–A172.
[31] X.J. Chen, S.H. Chan, K.A. Khor, Electrochim. Acta 49 (2004) 1851–1861.
[32] F. Zhao, A.V. Virkar, J. Power Sources 141 (2005) 79–95.
[33] N.T. Hart, N.P. Brandon, M.J. Daj, N. Lapeña Rey, J. Power Sources 106 (2002) 42–50.
[34] M. Suzuki, T. Oshima, Powder Technol. 44 (1985) 213–218.
[35] D. Bouvard, F.F. Lange, Acta Metall. Mater. 39 (12) (1991) 3083–3090.
[36] C.H. Kuo, P.K. Gupta, Acta Metall. Mater. 43 (1) (1995) 397–403.
[37] K.N. Grew, J.R. Izzo, W.K.S. Chui, J. Fuel Cell Sci. Technol. 8 (2011) 031001.
[38] D.A. Noren, M.A. Hoffmann, J. Power Sources 152 (2005) 175–181.
[39] R. Suwanwarangkul, E. Croiset, M.W. Fowler, P.L. Douglas, E. Entchev, M.A. Douglas, J. Power Sources 122 (2003) 9–18.
[40] R.B. Bird, W.E. Stewart, E.N. Lightfoot, Transport Phenomena, John Wiley and Sons, New York, 2002.
[41] P.D. Neufeld, A.R. Jansen, R.A. Aziz, J. Chem. Phys. 57 (1972) 1100–1102.
[42] B. Todd, J.B. Young, J. Power Sources 110 (1) (2002) 186–200.
[43] S. Kakac, A. Pramuanjaroenkij, X.Y. Zhou, Int. J. Hydrogen Energ. 32 (2007) 761–786.
[44] K. Fischer, J.R. Seume, J. Fuel Cell Sci. Technol. 6 (2009) 011002.
[45] M. Suzuki, T. Oshima, Powder Technol. 35 (1983) 159–166.